

---

# Semiconductor Quantum Dot Lasers

---

Authors:

Charles Christensen (s113046)  
Gandalf Saxe (s113093)

Advisors:

Anders Nysteen, DTU Fotonik  
Jakob Rosenkrantz de Lasson, DTU Fotonik  
Prof. Jesper Mørk, DTU Fotonik

Course Responsible:

Morten Bache, DTU Fotonik

# Abstract

Semiconductor quantum dots (QDs) have unique atom-like properties and are therefore often referred to as “man-made artificial atoms”. They have properties that make them useful for ultrafast communication lasers but are also being explored for future quantum information technology. Firstly we will solve numerically the three-dimensional Schrödinger equation for different QD systems related to the fabrication and modelling of quantum dots on a wetting-layer. The simulations are performed using COMSOL , where we calculate the eigenenergies and visualize the three-dimensional wave functions. Secondly we consider the application of quantum dots as active medium in a laser. In order to examine such a quantum dot laser, we derive and solve equations governing the dynamics of lasers, and we will then extend these equations by incorporating properties of QDs along with results from the numerical computations of QDs from COMSOL . We will also attempt to optimize quantum dot dimensions with respect to laser gain.

# Preface

This project is submitted as part of a mandatory course in the Physics and Nanotechnology Bachelor of Science in Engineering from the Technical University of Denmark (DTU). The project has been over the duration of one semester and awards 10 ECTS points.

## Acknowledgements

We would like to thank our project advisors Anders Nysteen, Ph.D Student at DTU Department of Photonics Engineering, Jakob Rosenkrantz de Lasson, Ph.D Student at DTU Department of Photonics Engineering and Jesper Mørk, Professor and Group Leader at Department of Photonics Engineering, Nanophotonics Theory and Signal Processing.

# Contents

<b>1</b>	<b>Introduction</b>	<b>1</b>
1.1	Fabrication . . . . .	2
1.2	Quantum dot lasers . . . . .	2
<b>2</b>	<b>Quantum wells – one-dimensional analogue</b>	<b>3</b>
2.1	Infinite quantum well . . . . .	3
2.2	Finite quantum well . . . . .	3
<b>3</b>	<b>The Schrödinger equation for conical quantum dots</b>	<b>6</b>
3.1	The Schrödinger equation for systems with azimuthal symmetry . . . . .	6
3.2	Separation of variables . . . . .	7
3.3	Wave function on coefficient PDE form . . . . .	7
<b>4</b>	<b>Numerical computations on conical quantum dots</b>	<b>8</b>
4.1	Utilizing COMSOL as a finite element analysis tool . . . . .	8
4.1.1	Model . . . . .	9
4.1.2	Results . . . . .	11
4.2	Convergence analysis . . . . .	13
4.2.1	Pure wetting layer . . . . .	13
4.2.2	Convergence in terms of mesh and scaling of computation domain . . . . .	14
4.3	Examination of quantum confinement . . . . .	16
4.3.1	Electron hole . . . . .	16
4.3.2	Confinement for higher energy states . . . . .	16
<b>5</b>	<b>Laser dynamics for quantum dot lasers</b>	<b>19</b>
5.1	The rate equations . . . . .	19
5.1.1	Deriving the rate equations . . . . .	19
5.1.2	Simulating the rate equations for a simple laser . . . . .	21
5.2	Implementation of quantum dot laser gain . . . . .	24
5.2.1	Envelope wave function overlap integral of electron and hole . . . . .	25
5.2.2	Optimization of gain from quantum dots . . . . .	25
5.2.3	Rate equations for quantum dot laser . . . . .	26
<b>6</b>	<b>Conclusion</b>	<b>30</b>
<b>7</b>	<b>Appendix</b>	<b>31</b>
7.1	Derivation for coefficient PDE form . . . . .	31
7.2	Ineffectiveness of high mesh fineness . . . . .	31
7.3	Envelope wave function . . . . .	31
7.4	Plots for probability density function . . . . .	35
7.5	Script for optimization of quantum dot laser gain . . . . .	35
7.6	Parameters for rate equations simulation . . . . .	39
7.7	Parameters and script for QD rate equations simulation . . . . .	39

7.8 QD Lasing Gain Threshold . . . . .	40
<b>References</b>	<b>42</b>

## Introduction

Quantum dots have been extensively studied in recent years because of their potential for technological applications. Briefly stated a quantum dot (QD) is a portion of matter whose excitons are confined in all three spatial dimensions. This means that an electron that is in the interior of a QD will experience a potential barrier in all directions. The dimensions of QDs usually range from 1 nm to 20 nm. They can be fabricated from many different kinds of semiconductor materials and in various geometrical shapes (cubes, spheres and cones for instance). All these opportunities can be utilized to achieve certain desirable properties of the QD – for example, by varying the size appropriately a QD can be produced with a very specific band gap making them ideal for optical applications, where it may be required that a certain wavelength of light is generated. In fact for laser applications QDs are so interesting that a whole field of research on quantum dot lasers have emerged. These quantum dot lasers have been theoretically predicted to possess properties by far superior to any other laser type since the early eighties [5] – the main advantages being that they require a low threshold current to operate, have a high laser gain, are very resistant to external temperature, and as mentioned can emit light at very well-defined wavelengths.

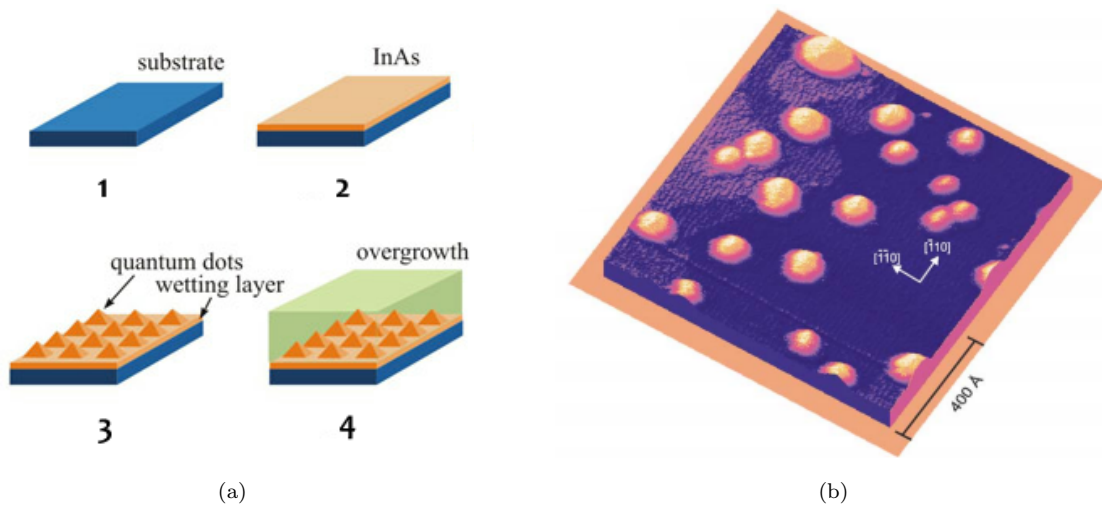


**Figure 1.1:** (a) Schematically depiction of the four steps in the process of QDs formation in Stranski–Krastanow regime. (b) 3-D STM (scanning Tunnel Microscope) image of InAs QDs on GaAs [6].

## 1.1 Fabrication

The fabrication of quantum dots has gone through various phases since its initial discovery in the late 70's and early 80's, including lithographic processes that create two-dimensional structures that could then be etched down to isolate the dot [10]. However a newer method that is usually the one used for lasers is to grow self-assembling dots by growing a layer of semiconductor material unto a wetting layer. The growth of quantum dots is based on a mismatch of lattice- and surface energy parameters that causes strain in material, which then pulls together resulting in “islands” of quantum dots. This is also known as Stranski-Krastanov growth, see figure 1.1(a). The main limitations of growing quantum dots this way are the cost of fabrication and the lack of control over positioning of individual dots, however significant efforts has been made to enable control of the dot size [11] [12]. Self-assembled dots are typically between 5 and 50 nm in size. By carefully choosing the semiconductor material, and if necessary dot it with other semiconductor materials, there is a high degree of control over the band gap and therefore operational frequency of quantum dot laser.

## 1.2 Quantum dot lasers

A quantum dot laser is a semiconductor laser that uses quantum dots as the active laser medium in its light emitting region.

Put shortly the quantum laser works by pumping electrons from the valence band of a QD to the conduction band leaving an electron hole in the valence band. Light is emitted when an electron in the conduction band recombines with an empty electron hole. When an electron and a hole recombines the energy of the emitted light will be equivalent to a certain band gap plus the energies of the valence band state and the conduction band state. When constructing QD lasers whole layers of QDs are often stacked upon each other in order to increase volumetric QD density, see fig. 1.2.

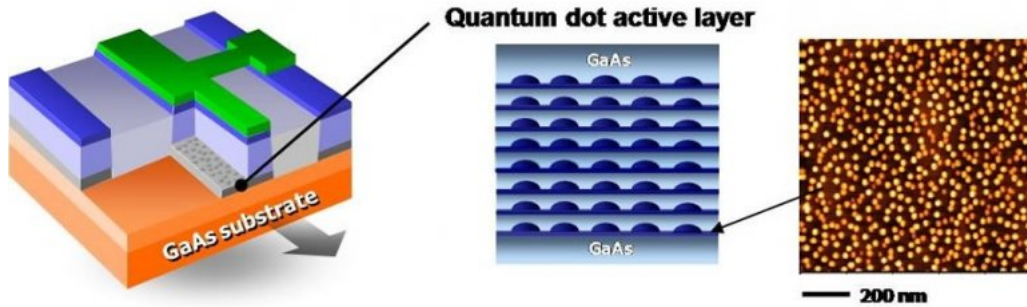


**Figure 1.2:** Quantum dot laser featuring an active layer containing high-density arrays of quantum dots.

## Quantum wells – one-dimensional analogue

In the following we will start off studying the simple case of an electron confined in a single dimension by means of potential barriers; a quantum well (QW). The knowledge attained from this one-dimensional instance will later serve as a benchmark for our numerical computations.

### 2.1 Infinite quantum well

We will consider an electron confined in one dimension by infinite potential barriers separated by a length  $L$  – in mathematical terms this can be put as

$$V(x) = \begin{cases} 0, & 0 < x < L, \\ \infty, & \text{otherwise.} \end{cases} \quad (2.1)$$

The absolute square of the wave function,  $\psi(x)$ , for the electron at a given position is proportional to the probability of finding the electron there. The wave function must therefore vanish everywhere beyond the edges of the potential well,  $\psi(|x| > L) = 0$ .

The function  $\psi(x) = A \sin(kx)$  satisfies these boundary conditions if  $k$  is such that  $kL = \pi n \Rightarrow k = \pi n/L$ , where  $n \in \mathbb{N}$ .

Furthermore the normalization condition must apply, meaning that  $\int_{-\infty}^{\infty} |\psi(x)|^2 dx = 1$ . This yields a requirement for the coefficient  $A$  that is found by evaluating the integral

$$\int_{-\infty}^{\infty} A^2 \sin^2\left(\frac{\pi n}{L}x\right) dx = 1 \Leftrightarrow \frac{1}{2}A^2L = 1 \Leftrightarrow A = \sqrt{\frac{2}{L}}. \quad (2.2)$$

The trigonometrical identity  $\sin^2 \theta = \frac{1}{2}(1 - \cos 2\theta)$  has been used to evaluate the integral.

The wave function for the electron has now been fully determined and the energy levels  $E$  can be found using the time-independent Schrödinger equation in one-dimension

$$-\frac{\hbar^2}{2m} \frac{\partial^2 \psi(x)}{dx^2} + V(x)\psi(x) = E\psi(x). \quad (2.3)$$

Evaluating the expression on the left-hand side of (2.3) and rearranging, we find that

$$E_{\text{inf}} = \frac{\hbar^2 \pi^2 n^2}{2m_i L^2}, \quad n \in \mathbb{N}. \quad (2.4)$$

### 2.2 Finite quantum well

We will now consider an electron confined in one dimension by finite potential barriers separated by a length  $L$ , see fig. 2.1, which is analogous to an electron moving in a region consisting of two



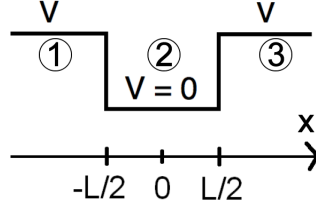


**Figure 2.1:** Illustration of a one-dimensional quantum well with the regions 1, 2 and 3.

different materials that are responsible for the electron experiencing two different potentials. We might as well assume that the electron also has a different effective mass in each of these materials. The time-independent Schrödinger equation in one-dimension is now slightly modified by introducing the position-dependent effective mass  $m_e(x)$ :

$$-\frac{\hbar^2}{2m_e(x)} \frac{\partial^2 \psi(x)}{dx^2} + V(x)\psi(x) = E\psi(x). \quad (2.5)$$

Assuming that regions 1 and 3 are of the same material, we can regard the effective mass in these regions as  $m_{\text{Ga}}$ , whereas the effective mass in region 2 can be regarded as  $m_{\text{In}}$ .

The wave function is now divided into three subfunctions for each of the regions shown in fig. 2.1

$$\psi = \begin{cases} \psi_1, & \text{if } x < -L/2 \\ \psi_2, & \text{if } -L/2 < x < L/2 \\ \psi_3, & \text{if } x > L/2 \end{cases}.$$

In the region  $-L/2 < x < L/2$  we have  $V = 0$  so (2.5) simplifies to

$$\frac{\partial \psi_2}{\partial x} = -\frac{2m_{\text{In}}}{\hbar^2} E \psi_2 = -\alpha^2 x, \quad (2.6)$$

where we have defined

$$\alpha = \frac{\sqrt{2m_{\text{In}}E}}{\hbar}. \quad (2.7)$$

The general solution to this differential equation is

$$\psi_2(x) = A \sin \alpha x + B \cos \alpha x. \quad (2.8)$$

In region 1 and 3 we have  $V = V_e$  and (2.5) becomes

$$\frac{\partial^2 \psi}{\partial x^2} = (V - E) \frac{2m_{\text{Ga}}}{\hbar^2} \psi = \kappa^2 \psi(x), \quad (2.9)$$

where we have defined

$$\kappa = \frac{\sqrt{2m_{\text{Ga}}(V_e - E)}}{\hbar}. \quad (2.10)$$

The general solution to the differential equation (2.5) is

$$\psi_1 = C e^{-\kappa x} + D e^{\kappa x}, \quad \psi_3 = F e^{-\kappa x} + G e^{\kappa x}. \quad (2.11)$$

It is clear that  $C = G = 0$ , since the terms containing these factors diverges far away from the quantum well, which is not in agreement with the normalization condition  $\int_{-\infty}^{\infty} |\psi(x)|^2 dx = 1$ .

The boundaries between regions are expected to be characterized by continuity and differentiability, so we can apply the boundary conditions  $\psi_1(-L/2) = \psi_2(-L/2)$ ,  $\psi_2(L/2) = \psi_3(L/2)$ ,  $\frac{d\psi_1}{dx}(-L/2) = \frac{d\psi_2}{dx}(-L/2)$  and  $\frac{d\psi_2}{dx}(L/2) = \frac{d\psi_3}{dx}(L/2)$ .

By direct computation these conditions imply that there are two types of solutions; either  $A = 0$  (symmetric modes) or  $B = 0$  (antisymmetric modes). For the case  $A = 0$  we also find that  $D = F$  and for the case  $B = 0$  we find  $D = -F$ . With these coefficient values the equations obtained from the boundary conditions reduces to a set of two linear independent equations for each mode.

For the symmetric modes we have the two equations  $De^{-\kappa L/2} = B \cos(\alpha L/2)$  and  $-\kappa De^{-\kappa L/2} = -\alpha B \sin(\alpha L/2)$  and by dividing these we obtain the following relation

$$\tan(\alpha L/2) = \frac{\kappa}{\alpha} \Leftrightarrow \tan\left(\sqrt{2m_i E} \frac{L}{2\hbar}\right) = \sqrt{\frac{V_e - E}{E}} \cdot \frac{m_i}{m_u} \quad (\text{symmetric modes}). \quad (2.12)$$

By similar insertion of the coefficients for the antisymmetric modes in the equations from the boundary conditions, we obtain the two linear independent equations  $De^{-\frac{\kappa L}{2}} = B \cos\left(\frac{\alpha L}{2}\right)$  and  $D\kappa e^{-\frac{\kappa L}{2}} = \alpha B \sin\left(\frac{\alpha L}{2}\right)$ , which by division leads to the relation

$$-\cot(\alpha L/2) = \frac{\kappa}{\alpha} \Leftrightarrow -\cot\left(\sqrt{2m_i E} \frac{L}{2\hbar}\right) = \sqrt{\frac{V_e - E}{E}} \cdot \frac{m_i}{m_u} \quad (\text{antisymmetric modes}). \quad (2.13)$$

The two nonlinear equations (2.12) and (2.13) can now be solved numerically in order to determine the allowed energies  $E$ .

## The Schrödinger equation for conical quantum dots

We will now consider the more advanced case of an electron confined to an azimuthal symmetric quantum dot (for instance a cone) placed upon a wetting layer. In general we will tend to use cylindrical coordinates, given by the axial coordinate  $z$ , the radial coordinate  $r$ , and the azimuthal angle  $\phi$ , unless otherwise specified.

### 3.1 The Schrödinger equation for systems with azimuthal symmetry

The one-band Schrödinger equation, with regard to an electron at position  $\vec{x}$ , is generally stated as

$$-\frac{\hbar^2}{2} \nabla \cdot \left( \frac{1}{m_e(\vec{x})} \nabla \psi(\vec{x}) \right) + V_e(\vec{x}) \psi(\vec{x}) = E \psi(\vec{x}), \quad (3.1)$$

where  $\hbar$ ,  $m_e(\vec{x})$ ,  $V_e(\vec{x})$ ,  $E$ , and  $\psi(\vec{x})$  respectively designates the reduced Planck's constant, the position-dependent electron effective mass, the potential energy, the electron energy, and the wave equation of the electron.

Let us now assume that the wave function is separable in terms of  $\phi$  so that

$$\psi(\vec{x}) = \chi(z, r) \Phi(\phi). \quad (3.2)$$

Using this form along with the assumption of cylindrical symmetry ( $V_e(\vec{x}) = V_e(z, r)$  and  $m_e(\vec{x}) = m_e(z, r)$ ) equation (3.1) can be written

$$-\frac{\hbar^2}{2} \nabla \cdot \left( \frac{1}{m_e(z, r)} \nabla \chi(z, r) \Phi(\phi) \right) + V_e(z, r) \chi(z, r) \Phi(\phi) = E \chi(z, r) \Phi(\phi) \quad (3.3)$$

At this point, for the sake of simplicity, we define  $\chi \equiv \chi(z, r)$ ,  $\Phi \equiv \Phi(\phi)$ ,  $V_e \equiv V_e(z, r)$  and  $m_e \equiv m_e(z, r)$ . Working out the gradient and divergence<sup>1</sup> of (3.3) we get

$$\begin{aligned} & -\frac{\hbar^2}{2} \nabla \cdot \left[ \frac{1}{m_e} \left( \Phi \frac{\partial \chi}{\partial r} \hat{\mathbf{r}} + \frac{1}{r} \chi \frac{\partial \Phi}{\partial \phi} \hat{\phi} + \Phi \frac{\partial \chi}{\partial z} \hat{\mathbf{z}} \right) \right] \\ & + V_e \chi \Phi = E \chi \Phi \end{aligned} \quad (3.4)$$

$$\begin{aligned} \Leftrightarrow & -\frac{\hbar^2}{2} \left[ \frac{\Phi}{r} \frac{\partial}{\partial r} \left( \frac{r}{m_e} \frac{\partial \chi}{\partial r} \right) + \frac{1}{r^2} \frac{\chi}{m_e} \frac{\partial^2 \Phi}{\partial \phi^2} + \Phi \frac{\partial}{\partial z} \left( \frac{1}{m_e} \frac{\partial \chi}{\partial z} \right) \right] \\ & + V_e \chi \Phi = E \chi \Phi. \end{aligned} \quad (3.5)$$

<sup>1</sup>Divergence:  $\nabla \cdot \mathbf{v} = \frac{1}{r} \frac{\partial}{\partial r}(rv_r) + \frac{1}{r} \frac{\partial v_\phi}{\partial \phi} + \frac{\partial v_z}{\partial z}$ , gradient:  $\nabla t = \frac{\partial t}{\partial r} \hat{\mathbf{r}} + \frac{1}{r} \frac{\partial t}{\partial \phi} \hat{\phi} + \frac{\partial t}{\partial z} \hat{\mathbf{z}}$ .

### 3.2 Separation of variables

We are now able to isolate the  $\phi$  term by multiplying (3.5) with  $\frac{m_e r^2}{\Phi \chi_n}$  and rearranging

$$\begin{aligned} & -\frac{\hbar^2 m_e r^2}{2} \left[ \frac{1}{r} \frac{\partial}{\partial r} \left( \frac{r}{m_e} \frac{\partial \chi_n}{\partial r} \right) + \frac{\partial}{\partial z} \left( \frac{1}{m_e} \frac{\partial \chi_n}{\partial z} \right) \right] \\ & + m_e r^2 (V_e - E) = \frac{\hbar^2}{2} \frac{\partial^2 \Phi}{\partial \phi^2} \frac{1}{\Phi} \equiv -\frac{\hbar^2}{2} n^2. \end{aligned} \quad (3.6)$$

Equation (3.6) has all terms depending on  $z$  and  $r$  and the term depending on  $\phi$  separated. Consequently, the expression on each side of equation (3.6) must correspond to a constant, since the equation holds for all possible values of  $z, r$  and  $\phi$ . Defining this constant as  $-\frac{\hbar^2}{2} n^2$ , we can focus on the two separate equations.

The general solution to the second order differential equation to the right of (3.6) is

$$\Phi = A \exp(in\phi) + B \exp(-in\phi) = C \cos n\phi + D \sin n\phi. \quad (3.7)$$

Since  $\Phi$  is a single-valued function we have the boundary condition  $\Phi(0) = \Phi(2\pi)$ , which can only be satisfied if  $n$  is an integer as seen clearly from the last expression in (3.7). For simplicity we choose the solution  $\Phi(\phi) = \exp(in\phi)$ .

Physically,  $n$  can be seen analogous to the atomic angular momentum quantum number<sup>2</sup> that is responsible for the diversity of atomic orbitals [13]. Interestingly, as we'll see later,  $n$  also gives rise to orbital-looking wave functions.

Regarding the  $z$  and  $r$  dependent terms of (3.6) we have the equation

$$-\frac{\hbar^2}{2} \left[ \frac{\partial}{\partial z} \left( \frac{1}{m_e} \frac{\partial \chi_n}{\partial z} \right) + \frac{1}{r} \frac{\partial}{\partial r} \left( \frac{r}{m_e} \frac{\partial \chi_n}{\partial r} \right) \right] + \frac{\hbar^2}{2} \frac{\chi_n}{m_e} \frac{n^2}{r^2} + V_e \chi_n = E \chi_n, \quad (3.8)$$

where the subscript  $n$  in  $\chi_n$  indicates that the electron envelope function now depends on  $n$ .

### 3.3 Wave function on coefficient PDE form

We now return to the separated version of the Schrödinger equation (3.8)

$$-\frac{\hbar^2}{2} \left[ \frac{\partial}{\partial z} \left( \frac{1}{m_e} \frac{\partial \chi_n}{\partial z} \right) + \frac{1}{r} \frac{\partial}{\partial r} \left( \frac{r}{m_e} \frac{\partial \chi_n}{\partial r} \right) \right] + \left( \frac{\hbar^2}{2} \frac{n^2}{m_e r^2} + V_e \right) \chi_n = E \chi_n. \quad (3.9)$$

In order to use this equation for numerical computation, we must bring it to a generalised form of a coefficient PDE (partial differential equation)

$$\nabla \cdot (-c \nabla u - \vec{\alpha} + \vec{\gamma}) + au + \vec{\beta} \cdot \nabla u = d_a \lambda u. \quad (3.10)$$

For these to be identical the coefficients are identified as  $u = \chi_n$ ,  $\alpha = \gamma = 0$ ,  $c = \frac{\hbar^2}{2} \frac{1}{m_e}$ ,  $a = \frac{\hbar^2}{2} \frac{n^2}{m_e r^2} + V_e$ ,  $\beta_r = -\frac{\hbar^2}{2} \frac{1}{m_e r}$ ,  $d_a = 1$  and  $\lambda = E$ . It is important to note that  $\nabla$  is not the divergence for cylindrical coordinates, but is a vector defined as  $\frac{\partial}{\partial r} \hat{\mathbf{r}} + \frac{\partial}{\partial z} \hat{\mathbf{z}}$ . To show that the equations are equal, the coefficients can be inserted in (3.10), however it is directly clear that  $au$  corresponds to the right term on the left-hand side (LHS) of (3.9), and that  $d_a \lambda u$  corresponds to the right-hand side (RHS) of (3.9), but it remains to be shown that  $\nabla \cdot (-c \nabla) + \vec{\beta} \cdot \nabla u$  is equal to the first term on the LHS of (3.9). This is shown in app. 7.1.

---

<sup>2</sup>Often denoted  $l$  and represented by  $s, p, d$  and  $f$  for  $l = \{0, 1, 2, 3\}$ , respectively.

# Numerical computations on conical quantum dots

COMSOL Multiphysics is a finite element analysis, solver and simulation software package for various physics and engineering applications, especially coupled phenomena, or multiphysics. COMSOL Multiphysics also offers an extensive link to MATLAB with toolboxes for a wide variety of programming, pre-processing and post-processing possibilities. Given that COMSOL offers a quick and easy platform for setting up various configurations involving quantum dots, we will mostly be using this tool to build our models and then subsequently transfer these models to MATLAB in order to automate calculations and post-process data.

In general we will restrict our study to systems of azimuthal symmetry; thus in defining the geometry of a system, we will only have to consider a cross-section in the  $rz$ -plane so that the whole system is produced by azimuthal rotation. In addition, systems of azimuthal symmetry only require a two-dimensional numerical approach since  $\psi(r, z, \phi) = \chi(z, r) \exp(in\phi)$ , as we learned in section 3.1.

We will begin this chapter with the study of a conical quantum dot. Firstly the numerical model based on the FEM (finite element method) is described and utilized to obtain results. These results will then be analyzed in terms of convergence behaviour and various visualisations. After this has been carried out, we will draw a parallel to the theoretical work done in section 2.1 and 2.2 in order to access how well the numerical model converge towards the expected analytical values in the case of a quantum well system (the pure wetting layer).

## 4.1 Utilizing COMSOL as a finite element analysis tool

With the use of COMSOL we will solve the separated form of the Schrödinger equation (3.8) for the conical QD system. As we'll see it is fairly easy to account for different potentials and effective masses in separate domains of a system by virtue of FEM.

There are basically two domains that we will be considering; the QD/WL (wetting layer) domain and the exterior. The wetting layer is the substrate upon which the quantum dots are grown. The layer is made of the same material as the quantum dot, typically InAs, and the composition of the wetting layer (WL) and QD is, as described in the introduction, embedded in another material, typically GaAs. The fact that the WL and the QD are of the same material result in the electron having an equal potential energy  $V_{\text{In}}$ , wherever it is in the composite QD/WL domain. The surrounding GaAs, however, give rise to another potential  $V_{\text{Ga}}$ , which is higher than  $V_{\text{In}}$ . Consequently the electron tends to reside in the QD/WL domain.

### 4.1.1 Model

#### Geometry

In terms of the numerical FEM model we have to define a system of finite size in order to simulate the QD system. This means that we have to cut off the wave function at some point, which adds additional uncertainty to the FEM model.

In order to proceed with COMSOL we therefore settle for a sufficiently large size of the entire cross-section area; this area is referred to as the computation domain (CD). Initially we will look upon a  $50 \text{ nm} \times 100 \text{ nm}$  sized CD containing a conical QD (of different dimensions) grown on a 2 nm WL, see fig. 4.1(a).

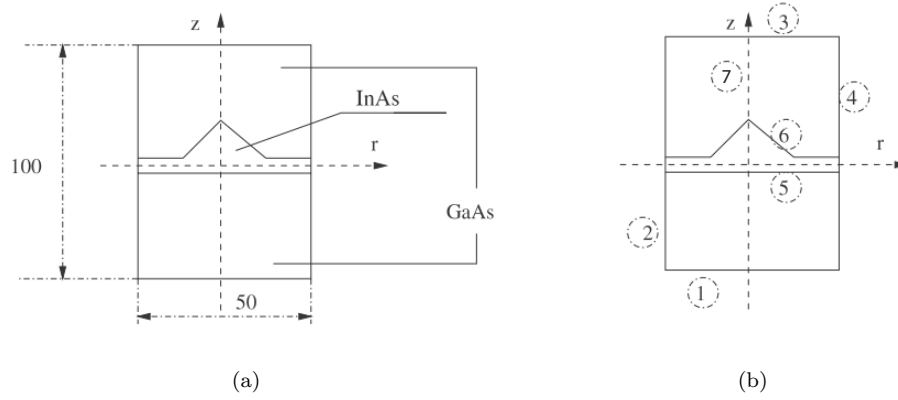


**Figure 4.1:** Depictions of the underlying geometry in the numerical COMSOL model. All length units are in nm. (a) The type of QD system we will study. In general the wetting layer (WL) will have a thickness of 2 nm, and the QD dimensions will be varied and so will the computation domain (CD). (b) Numbering of the respective boundaries. Due to symmetry boundary 2 can be set identical to boundary 4.

#### Boundary conditions

In order to obtain a stable and reliable numerical model it is necessary to determine which boundary conditions apply to the system. For this purpose we will treat the boundaries shown in 4.1(b).

There are basically three types of boundary conditions we will apply: Dirichlet boundary conditions,  $\chi = 0$ ; Neumann conditions,  $\frac{\partial}{\partial x}\chi = 0$  ( $x$  denotes the direction normal to the boundary); and finally we will also have to apply periodic boundary conditions to internal boundaries in order to ensure continuity of the envelope wave function.

Firstly, the boundaries 2 and 4 must be identical due to azimuthal symmetry. Since we are only interested in states confined to the QD, the wave equation will decay towards all of the boundaries 1, 2, 3 and 4, so in principle it shouldn't matter whether Dirichlet or Neumann conditions are employed provided that the computation domain is sufficiently large. However, for very small QDs the extent of the wave function (along the wetting layer) can easily become unmanageable in terms of meeting a CD of the required size (this is referred to as quasi-confinement). Wave functions that are vaguely localized in this manner are for practical reasons undesirable, so in order to distinguish them from the localized states, we will use Neumann conditions at boundary 2 and 4.

Quasi-confinement only occurs along the wetting layer so for boundary 3 and 4 we can choose either Dirichlet or Neumann conditions – Dirichlet conditions are chosen.

At the internal boundaries 5 and 6 periodic boundary conditions are employed. This ensures continuity of  $\chi_n(z, r)$ ,  $\frac{1}{m_e(z, r)} \frac{\partial}{\partial z} \chi_n(z, r)$  and  $\frac{r}{m_e(z, r)} \frac{\partial \chi_n}{\partial r}$  at the material boundaries.

Boundary 7 calls for a closer look at equation (3.8):

$$\frac{\partial}{\partial z} \left( \frac{1}{m_e} \frac{\partial \chi_n}{\partial z} \right) + \frac{1}{r} \frac{\partial}{\partial r} \left( \frac{r}{m_e} \frac{\partial \chi_n}{\partial r} \right) - \frac{\chi_n}{m_e} \frac{n^2}{r^2} = \frac{2}{\hbar^2} (E - V_e) \chi_n, \quad (4.1)$$

where the second and third term diverge unless boundary conditions are employed. We recall that the effective mass is a dependent variable:  $m_e(z, r)$ . Assuming that the effective mass is invariable infinitesimally close to boundary 7, the second and third term of (4.1) becomes

$$\frac{1}{m_e} \left( \frac{1}{r} \frac{\partial \chi_n}{\partial r} + \frac{\partial^2 \chi_n}{\partial r^2} - \chi_n \frac{n^2}{r^2} \right). \quad (4.2)$$

When  $n = 0$  the third term of (4.2) vanishes, so for the first term not to diverge a Neumann condition must be implemented;  $\frac{\partial}{\partial r} \chi_n(z, r) = 0$ .

For  $n = 1$  the third term becomes  $-\chi_n \frac{1}{r^2}$ , whereas the first term is given by  $\frac{1}{r} \frac{\partial \chi_n}{\partial r}$ , which for  $r \rightarrow 0$  simplifies to  $\frac{1}{r} \frac{\chi_n(z, r) - \chi_n(z, 0)}{r} \big|_{r \rightarrow 0}$ . By imposing a Dirichlet condition at boundary 7,  $\chi_n(z, 0) = 0$ , it is seen that the first term of (4.2) cancels with the third term in the limit  $r \rightarrow 0$ , and thus the divergence of both terms is circumvented.

For the case  $n \geq 2$  the first and third term of (4.2) are not able to cancel, and hence both Dirichlet and Neumann conditions are imposed at boundary 7 ensuring that both terms equal zero when  $r \rightarrow 0$ .

### Coefficient Form PDE

Having set up the geometry of the system and knowing the boundary conditions, the different domains can now be given their respective physical characterization. This is done by assigning domain-dependent values to the coefficients in the general PDE equation (3.10):

$$\nabla \cdot (-c \nabla u - \vec{\alpha} + \vec{\gamma}) + au + \vec{\beta} \cdot \nabla u = d_a \lambda u. \quad (4.3)$$

As we learned in section 3.3 the coefficients  $c, a$  and  $\beta_r$  are defined as  $c = \frac{\hbar^2}{2} \frac{1}{m_e}$ ,  $a = \frac{\hbar^2}{2} \frac{n^2}{m_e r^2} + V_e$  and  $\beta_r = -\frac{\hbar^2}{2} \frac{1}{m_e r}$ .

For the QD/WL domain, referred to as the indium domain (In), we specify the exact values of these coefficients in COMSOL – and likewise for the exterior domains (the upper and lower surroundings), referred to as the gallium domain (Ga). The variable quantities in the above-mentioned coefficients are the potential  $V$  and the mass  $m$ ; thus, we introduce  $m_{\text{In}}, V_{\text{In}}, m_{\text{Ga}}$  and  $V_{\text{Ga}}$ . These parameters are material-specific and according to [8] they can be set to  $V_{\text{In}} = 0$ ,  $m_{\text{In}} = 0.027m_e$ ,  $m_{\text{Ga}} = 0.0665m_e$  and  $V_{\text{In}} = 0.697 \text{ eV}$ .

### Constructing an appropriate mesh

The final step of preparing the model for computation is building a mesh; the cornerstone of the FEM method. The mesh is built upon the implemented geometry with a specific mesh fineness. The fineness is essential for the resulting accuracy of the computations. However, the number of grids in the mesh is proportional to the computation time, and thus it is crucial to obtain the most efficient mesh. Additionally, choosing an appropriate computation domain (CD) is also of great importance, since a bigger CD requires more grids for the fineness not to deteriorate.

In order to obtain an efficient mesh an important notice is that it is far superior to use the concept of mesh refinements as opposed to increasing the mesh fineness equally in an entire geometry (same grid density everywhere), since regions of geometrical complexity require more grids for accurate computations. In addition to this it is also useful to allocate more mesh refinements to certain domains. In COMSOL we will therefore in general settle for a poor fineness (given that fineness improves an entire geometry uniformly) and then apply mesh refinements. See figure 4.2 for a deeper explanation of mesh refinements.

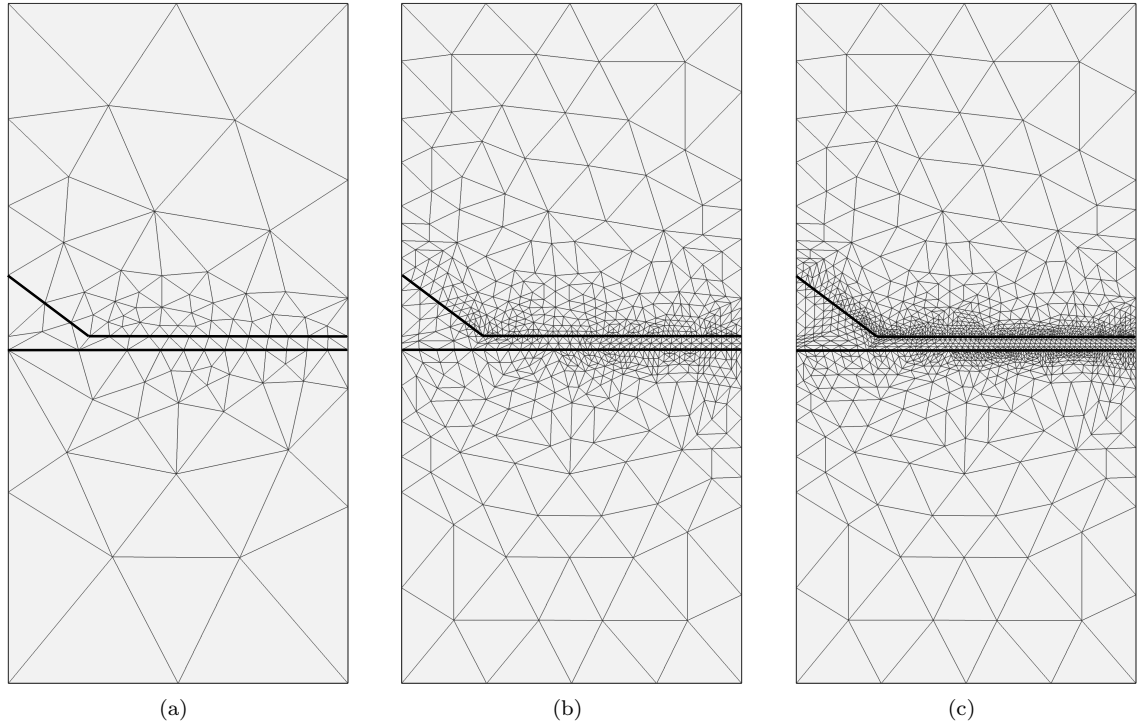


**Figure 4.2:** Illustrations of different mesh refinements. A single refinement splits every existing grid in the mesh into four equal triangles, so for each value the number of refinements increase the total number of grids increases by a factor of 4 (this is only approximate though, since the function of mesh refinement is more complicated at boundaries between different domains). Initially the three meshes are build with an extremely coarse fineness (as defined by COMSOL ) – from this point mesh refinements are added. (a) No refinements, only the initial extremely coarse mesh with 172 grid elements in total. The grid density is somewhat higher in the QD/WL area (which is why subsequent refinements are effective), however increasing the fineness further does not strengthen this tendency (see app. 7.2 for an example of this). (b) All domains refined once, 1259 grids in total. (c) Domain-specific refinement – an efficient technique for achieving high precision. QD/WL refined twice, exterior refined once, 2719 grids in total.

#### 4.1.2 Results

The computed data from COMSOL includes eigenenergies (the  $E$  from eq. (3.8) ) and function values of  $\chi(z, r)$ . A computation for a QD of 10 nm height and 20 nm width (base radius) has been done and the resulting data is plotted in fig. 4.3. Note that there are multiple solutions associated with each value of  $n$ ; there is a ground state (with lowest eigenenergy) and up to several excited states.

From section 3.1 we know that the envelope wave function is produced by multiplying  $\chi(z, r)$  with the angular dependent expression  $\Phi(\phi) = \exp(in\phi)$ . This is done in MATLAB for a Cartesian coordinate system, and the resulting wave function for two different values of the quantum number  $n$  is plotted in fig. 4.4.

The script used to build up the wave function from  $\chi(z, r)$  and  $\Phi(\phi)$  and convert from cylindrical to Cartesian coordinates can be seen in app. 7.3 – note that interpolation is used to evaluate the value of the wave function in arbitrary points.

In figure 4.4(a) we see a clear resemblance to atomic orbitals; more specifically the wave function in 4.4(a) with  $n = 0$  is very equivalent to atomic  $g$ -orbitals ( $l = 0$ ), whereas the wave function in 4.4(b) with  $n = 4$  clearly resembles atomic  $d$ -orbitals ( $l = 4$ ) [13]. In atomic physics what differs



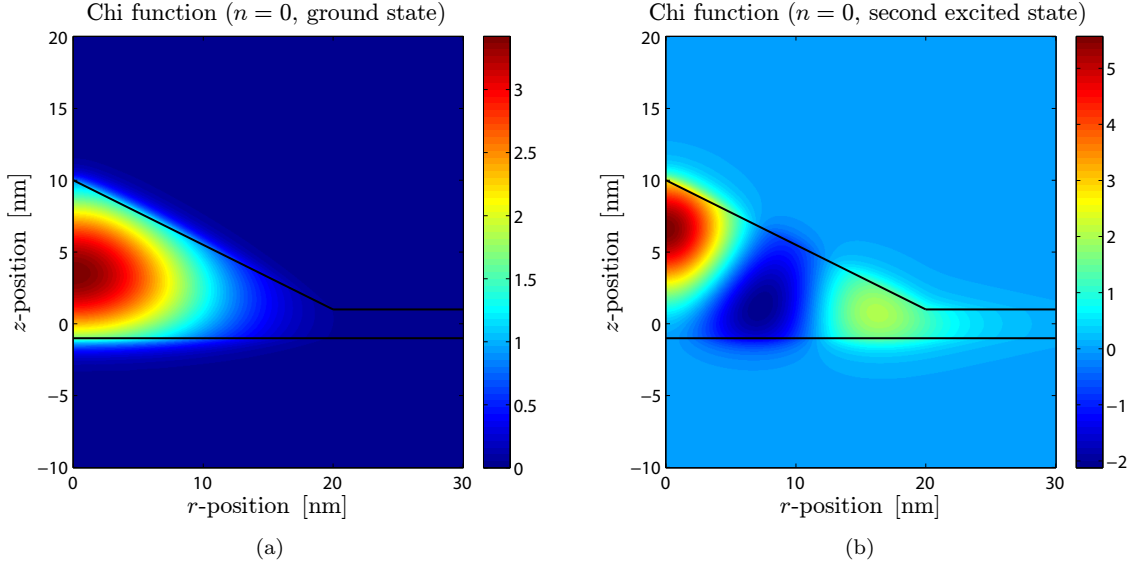


**Figure 4.3:** Visualization of numerical solution of  $\chi(z, r)$  from COMSOL simulation. The colorbar represents the value of  $\chi(z, r)$ . The black outline, representing the QD/WL, illustrates how the solutions are confined to the QD. The simulated QD has a height of 10 nm and a width of 20 nm. (a) Ground state belonging to  $n = 0$ , the eigenenergy is found to be  $E = 0.1223$  eV. (b) Third mode for  $n = 0$ , eigenenergy is  $E = 0.3516$  eV.

the  $s, p, d, f$  and  $g$  (etc.) orbitals is the angular momentum quantum number often denoted  $l$  – the orbitals correspond to  $l = \{0, 1, 2, 3, 4\}$ . Thus, for good reason the quantum number  $n$  can be regarded as the exact analogue to  $l$ . Moreover, quantum dots can in general be thought of as artificial atoms, given that they display the same physical behaviour. Mathematically speaking this similarity is not shocking, since both atoms and QDs are governed by Schrödinger's equation. In this view the atomic orbitals and the computed QD wave function are only just solutions to the same equation, but pertaining to different geometries. In any case it is remarkable that man-made constructions like QDs (that are relatively big) exhibit atom-like appearances.

The envelope wave function may be used to calculate the spatial probability density function given by  $|\psi(\vec{x})|^2$ . This quantity is used to normalize the wave function, since it is a requirement that  $\int |\psi(\vec{x})|^2 dV = 1$  (where we integrate over all space). Thus, we might have to scale  $\chi(z, r)\Phi(\phi)$  with a constant  $A$  for  $\psi(\vec{x})$  to be normalized. In cylindrical coordinates this yields

$$\begin{aligned}
 \int |\psi(\vec{x})|^2 dV &= \int_0^\infty \int_{-\infty}^\infty \int_0^{2\pi} |A\chi(z, r)\Phi(\phi)|^2 r d\phi dz dr \\
 &= A^2 \int_0^{2\pi} |\Phi(\phi)|^2 d\phi \int_0^\infty \int_{-\infty}^\infty |\chi(z, r)|^2 r dz dr \\
 &= 2\pi A^2 \int_0^\infty \int_{-\infty}^\infty |\chi(z, r)|^2 r dz dr = 1.
 \end{aligned} \tag{4.4}$$

The integral of  $|\Phi(\phi)|^2$  evaluates to  $2\pi$ , since  $|\Phi(\phi)|^2 = \overline{\Phi(\phi)}\Phi(\phi) = \exp(in\phi)\exp(-in\phi) = 1$ . The double integral of  $|\chi(z, r)|^2 r$  can be approximated numerically by a Riemann sum and the scaling factor  $A$  can then be found by means of (4.4). Normalizing the wave function will be necessary in certain later calculations, especially in the overlap integral that we'll address in a following section. Furthermore, when the normalization has been carried out the probability density function can be used to calculate the probability of finding the electron in a certain sub-volume  $\Omega$  by doing the volume integral  $\int_\Omega |\psi(\vec{x})|^2 dV$ , where  $dV = r d\phi dz dr$  for cylindrical coordinates. Since  $r$  is part of

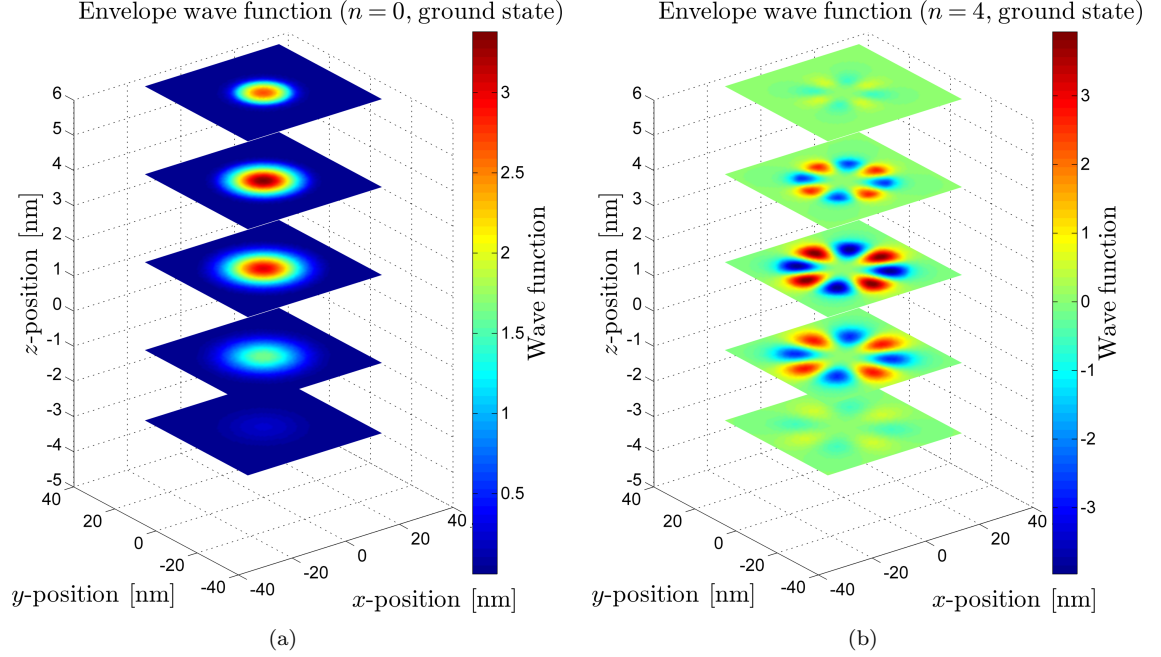


**Figure 4.4:** Horizontal slices of the envelope wave function for  $n = 0$  and  $n = 4$ . Due to the angular dependency  $\exp(in\phi)$  the quantum number  $n$  gives rise to exactly  $n$  oscillations in a full azimuthal rotation of  $2\pi$ . (a) Ground state belonging to  $n = 0$ , the eigenenergy is found to be  $E = 0.1223$  eV. (b) Ground state for  $n = 4$ , eigenenergy is  $E = 0.3517$  eV. Notice that precisely 4 oscillations are completed in a full azimuthal rotation.

this expression, the probability of finding an electron near the center of a QD is very low contrary to what could have been thought initially by considering figure 4.4(a). The equivalent figures of 4.4(a) and 4.4(b) for the probability integrand,  $|\psi(\vec{x})|^2 \cdot r$ , can be seen in app. 7.4.

## 4.2 Convergence analysis

Having established a numerical model in COMSOL and extracted solutions, we will have to make a confirmation that the solutions are valid and subject to insignificant errors. Such confirmation is ideally done by comparison with experimental data, and analytical values, and simply by comparing accurate computations with ones that are less accurate.

In this section we will investigate whether the numerical results converge towards analytical values under certain circumstances. Additionally we will test if the cut-off error (resulting from limiting the CD [computation domain]) is of any significance – if so, the resolution is to simply increase the CD.

### 4.2.1 Pure wetting layer

In this section we will consider the case of a pure wetting layer (WL), i.e. no quantum dots have been grown.

An electron will experience a lower potential energy in the WL than in the surrounding material, and given that the wetting layer is considered an infinitely large plane, the situation of a pure WL corresponds precisely to that of a quantum well (QW) as studied in section 2.1 and 2.2.

In order to compare the numerical model with analytical QW solutions we will let the height and width of the QD be zero and test if the computed eigenenergies converge towards the theoretical

energies from sec. 2.2, when computation accuracy is improved. Besides we will also make a test to see if this is also valid for the limit of  $V_{Ga} \rightarrow \infty$ , which corresponds to the infinite quantum well of sec. 2.1. We will also let  $n = 0$  in the numerical model, since the pure WL has two axes of symmetry, whereas  $n$  was introduced for a system of only azimuthal symmetry. Setting  $n = 0$  in (4.2) and imposing the  $r$  and  $\phi$  symmetry directly leads to the version of the Schrödinger equation used in solving the QW.

Setting the QD height/width and  $n$  to zero and using the potentials  $V_{Ga} = 0.697$  eV (as earlier) and  $V_{Ga} = 10^{10}$  results in the plots of figure 4.5. The high value of  $V_{Ga} = 10^{10}$  is used to simulate  $V_{Ga} \rightarrow \infty$ .

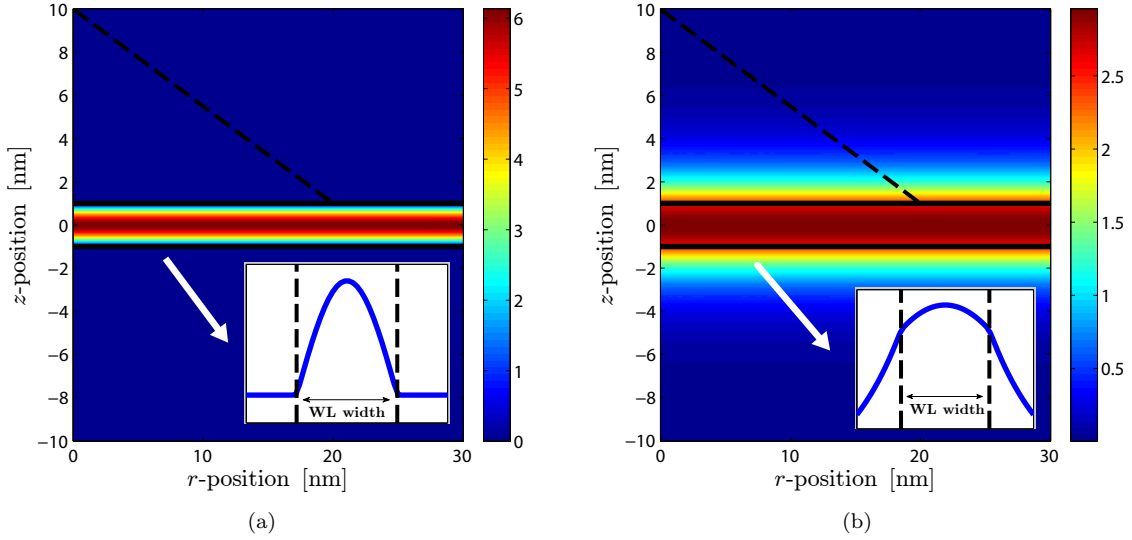


**Figure 4.5:** Solutions for pure wetting layer (WL) – the model used to compute these solutions is exactly the same as for the QD; the difference being that the height of the QD is set to zero, other than that all parameters are the same, including the WL width. The dotted line indicates the outline of the QD simulated earlier for comparison. (a) The potential outside the WL is set to infinity; corresponding to the infinite quantum well (see sec. 2.1). The computed eigenenergy is 3.482. (b) The potential outside the WL is set to  $V_{Ga} = 0.697$  eV (same as for the simulated QDs). The computed eigenenergy is 0.384 eV.

As expected the solutions are symmetric along the  $r$ -axis only varying across the WL just like solutions to the QW only varies in one dimension. It is also evident that the infinite potential outside the WL in fig. 4.5(a) makes the wave function reside exclusively inside the WL as opposed to fig. 4.5(b), where the wave function falls off exponentially outside the WL. The computed ground state eigenenergy for the infinite QW, 3.482 eV, is remarkably higher than the eigenenergy for the finite QW, 0.384 eV. This is not surprising since squeezing the wave function inside the WL by virtue of high exterior potential should intuitively give rise to higher energies.

#### 4.2.2 Convergence in terms of mesh and scaling of computation domain

With the results of sec. 4.2.1 we can now proceed to the convergence study of computed eigenenergies versus analytical eigenenergies. The analytical values are found to be 0.384199 eV and 3.481763 eV for the infinite and finite QW, respectively. The relative deviations to these values for computed eigenenergies resulting from computations of different mesh refinements are shown in fig. 4.6(a).

It is evident from fig. 4.6(a) that the numerical model approaches the analytical values, when the mesh density is increased – given that the CD is sufficiently large (a CD of  $25 \times 25$  nm<sup>2</sup> has been

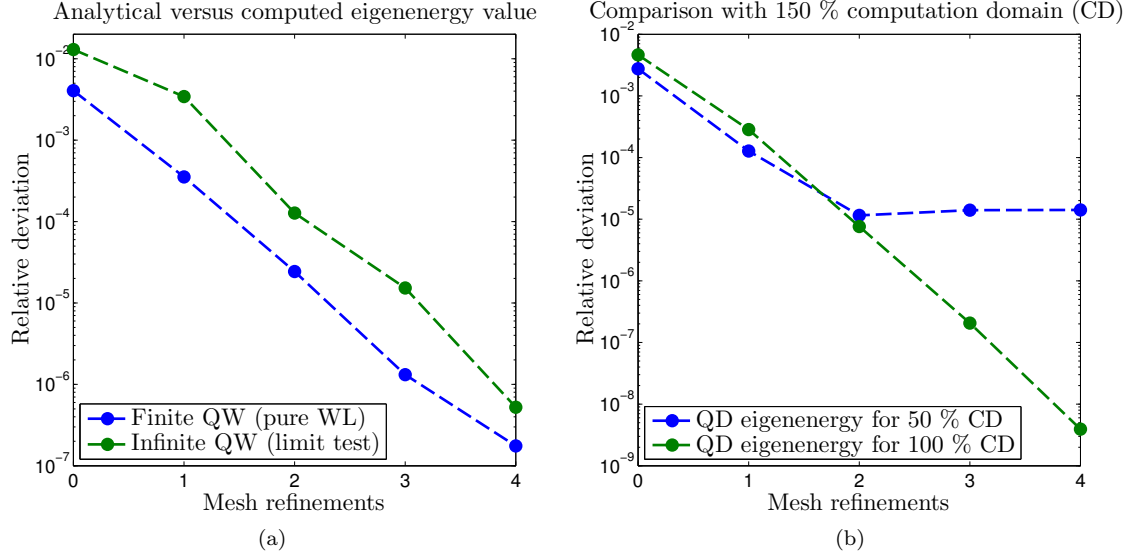


**Figure 4.6:** Convergence tests for the numerical COMSOL model. Both plots show deviation on computations for the ground state energy for  $n = 0$  relative to either an analytical value (left plot) or a more precise value (right plot) on a logarithmic axis; the variable parameter being the number of mesh refinements. For simplicity the mesh refinements are not domain specific, and thus apply to the whole geometry of the computation domain (CD) – note that the grid density resulting from refinements is independent on the size of the CD. (a) The blue graph shows the deviation between eigenenergy values obtained from the numerical computation relative to the analytical eigenenergy for the finite QW. For the numerical model to produce these eigenenergies the QD is set to have a height and width of zero (a pure WL). The green graph is analogous, but tests the convergence in the limit where the potential outside the WL ( $V_{Ga}$ ) goes to infinity (corresponding to the infinite QW). (b) This convergence test verifies that the error subject to cutting off the CD at a given height and width is negligibly small. In order to examine this we have computed the  $n = 0$  ground state eigenenergy for a QD of 3.6 nm height and 12 nm width in an excessively big CD of 150 % the size of a  $25 \times 25 \text{ nm}^2$  CD using 4 mesh refinements. However we see that a CD 100 % in size converges very closely towards the value found for a 150 % CD; thus the cut-off error is negligible when using a 100 % CD.

used for consistency, although we could have just used a much smaller width since there is symmetry in  $r$ ).

The size of the CD necessary for accurate calculations for the pure WL is obviously much lower than what is needed for calculations for a QD, because a QD extends to some height and width. For a QD of the 3.6 nm height and 12 nm width, we have therefore examined if computed eigenenergies are any different for a CD of 150 % the area  $25 \times 25 \text{ nm}^2$  compared to CDs only 50 % and 100 % of this area. The results from this examination are summarised in fig. 4.6(b). For the given QD we conclude that the 100% CD is sufficiently large, since the 100 % CD results in virtually the same  $n = 0$  ground state energy, when the number of mesh refinements are equal.

Note that for bigger QDs than the one simulated larger CDs may be needed, but the same convergence test can be carried out in such a case.

To sum up above findings we see clear indications that our numerical model yields valid solutions and the errors subject to the finite number of grids and the limited CD can be made negligible.

### 4.3 Examination of quantum confinement

Understanding the details of a quantum dots ability to confine an electron is important for being able to utilize them in laser applications. In this section we will study what determines whether an electron is confined or not. We will also introduce the concept of the electron hole, since the electron hole helps to demonstrate what determines quantum confinement. Also the electron be a necessary concept for simulating the QD laser later in this report.

#### 4.3.1 Electron hole

The electron hole is the mathematical opposite of an electron. It does not have any physical ground, but is useful for theoretical calculations. It is introduced when an electron is excited into a higher state. When this excitation happens it will leave a hole in its old state. To account for the influence that results from the electron not being in its previous state, the hole can be modelled as a particle that is attributed an effective mass and charge (opposite the electron charge). The hole has its own wave function, which can be used in calculating the effect of the hole. The effective mass of the hole is in general much higher than the effective mass of the electron [3]. Later in this section we will consider the confinement of the hole.

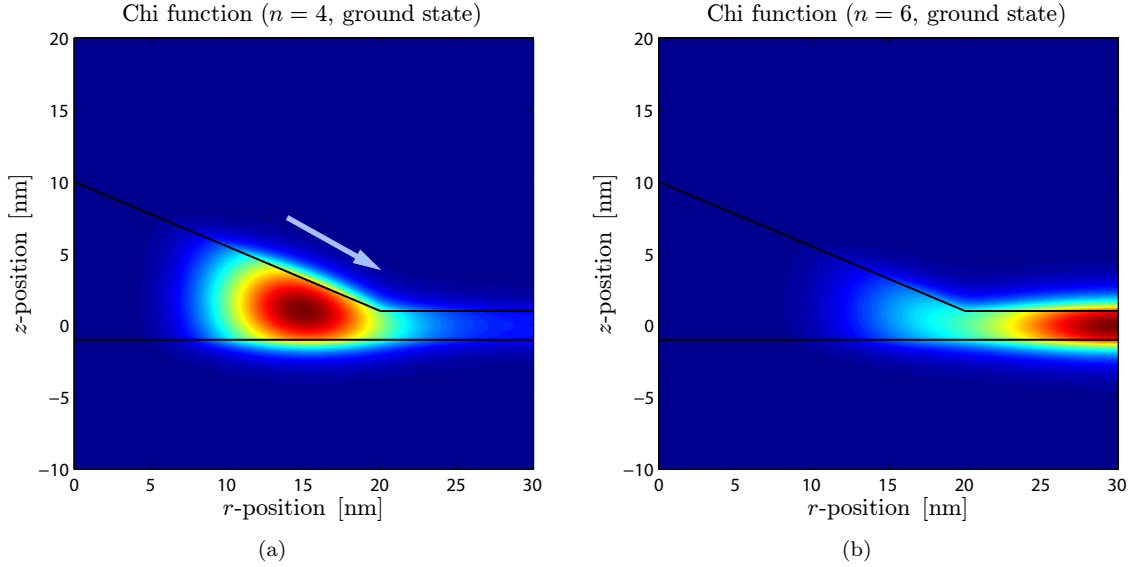


**Figure 4.7:** Confinement dependence on eigenenergy. The tendency to delocalization towards the WL progresses gradually as the wave function eigenenergy approaches the energy of the pure WL. Computed eigenenergies above that of the pure WL represent free energy states – these eigenenergies approach the pure WL eigenenergy asymptotically for increasing computation domain. (a) Ground state belonging to  $n = 0$ , the computed eigenenergy is 0.3572 eV. (b) Ground state for  $n = 0$ ; for the given QD this is a free energy state residing in the WL, the computed eigenenergy is 0.4092 eV.

#### 4.3.2 Confinement for higher energy states

A first quantitatively examination regarding electron confinement concerns higher energy states. The ground states that we have considered earlier have all been clearly confined to the simulated QD. One remark to take away from this observation is that the lowest energy states of the electron reside in the QD. An interpretation of this could be that the wave function is less squeezed in the volume of the QD than it otherwise would have in the WL, which results in the lower energy. For this reason

bigger QDs correspond to lower eigenenergies of the electron. Since the QD is associated with lower eigenenergies for states that are confined, one could imagine states that simply have too high energy to reside in the QD. This is exactly the case; increasing the quantum number  $n$  leads to less confined states. A higher  $n$  corresponds to more oscillations around the azimuthal plane, which amounts to a higher eigenenergy, so for higher  $n$  we expect to see less confinement. This is the essence of fig. 4.3.

Also since smaller QDs correspond to higher eigenenergies, it is not surprising that if the QD becomes small enough it will no longer offer a lower eigenenergy than the WL, and hence the ground state would preferably reside in the WL. This is also evident in fig. 4.7, since the confined state on fig. 4.7(a) has an eigenenergy of 0.357 eV, whereas the pure WL energy (the infinite QW) has an energy of 0.384 eV. On the other hand the energy state on fig. 4.7(b) has an eigenenergy of 0.409 eV surpassing the WL energy and as a consequence the state is not confined and therefore free.

We have now established that higher energies cause less confined states and ultimately free states. However, we have not identified which specific parameters determine the degree of confinement. It seems natural that the potential exterior to the QD ( $V_{\text{Ga}}$ ) plays a decisive role for the confinement. As we saw for the infinite QW, fig. 4.5(a), the wave function is squeezed into the WL because of the high exterior potential. The same is valid for QDs; if  $V_{\text{Ga}}$  is somehow increased the wave function is repelled additionally from the GaAs making it more likely that the wave function will reside in the QD. In fact the free ground state for  $n = 6$  on fig. 4.3(b) becomes confined if the  $V_{\text{Ga}}$  is increased from the usual 0.697 eV to around 1.7 eV.

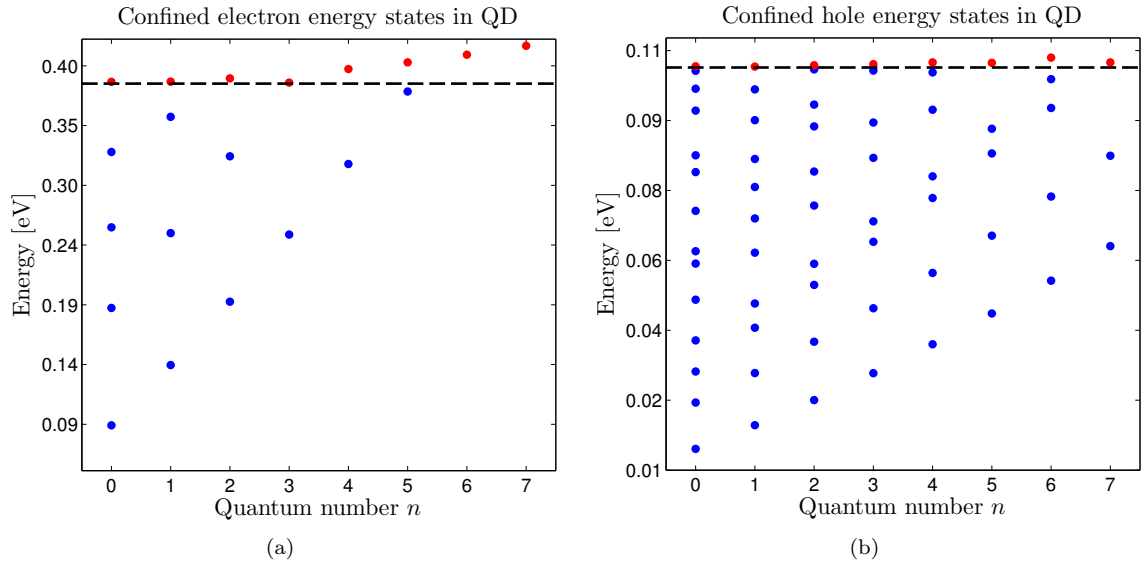


**Figure 4.8:** Comparison of confinement for the electron versus hole in a QD of 15 nm height and 20 nm width. The red dots represent the first unconfined state for each respective  $n$ . The dotted line represents the pure WL energy. (a) Confined electron states in the QD. The WL energy is 0.384 eV as earlier. Also notice the much higher eigenenergies. (b) Confined electron states in the QD. The WL energy for the hole is found to be 0.107 eV. Notice the far higher number of confined states.

Apart from the exterior potential another important parameter regarding the degree of confinement is the effective mass that a particle experiences in the different materials. If the effective mass inside the QD/QW domain is increased it might not be obvious what this will do for the confinement. But for the simple case of a quantum well we know that the energy is inversely proportional to the mass, see eq. (2.4). From this we could expect that eigenenergies are lower for more massive particles and hence more confined. Returning to electron holes and computing the eigenenergies for different quantum numbers, we see that this relation to the effective mass is true. Using the effective

masses  $m_{\text{In}}^* = 0.34m_e$  and  $m_{\text{Ga}}^* = 0.38m_e$  and the potential  $V_{\text{Ga}}^* = 0.368\text{ eV}$  for the hole and the earlier stated electron parameters, we obtain the results of fig. 4.8, where it is very apparent that the hole has lower eigenenergies and a lot more confined states. The figure also shows the dividing line between confined and free states by the energy of the pure WL.

## Laser dynamics for quantum dot lasers

All types of lasers consists of three basic components [2] [9]:

**Active laser medium** Also called gain medium. Where stimulated emission of photons occurs. The active medium has the property that passing photons will stimulate electrons to fall from the conductive band to the valence band of the material atoms. The active medium is an active component; external energy is transferred to the medium in the form of charge carriers (electrons and electron-holes). In our case quantum dots are the active medium.

**Pump source** The energy source that somehow adds external energy to the lasing process. In our case the pump mechanism is an electrical current causing electron collisions thereby creating charge carriers in the conductive band of the quantum dots. Thus the quantum dots are primed for stimulated coherent photon emission.

**Optical resonator system** The part of the laser that ensures that the stimulated light does not escape the laser device immediately, but returns to stimulate more photons. In most lasers this is an optical cavity consisting of two mirrors, one fully reflective and the other slightly partially reflective.

### 5.1 The rate equations

#### 5.1.1 Deriving the rate equations

We will now derive the rate equations governing the time evolutions of the *charge carrier volume density*  $N$  and *photon volume density*  $N_p$  within the active medium [4]. When a current is applied through the active medium several things will happen that will result in the gain of electrons and in recombination of electrons and electron-holes within the active medium. Our reference point will be the rate equation:

$$\frac{dN}{dt} = G_{gen} - R_{rec} \quad (5.1)$$

where  $G_{gen}$  is the rate of injected electrons per unit volume in the active region,  $R_{rec}$  is the total loss of charge carriers, the rate of recombining per unit volume in the active region. We wish to define a few terms relating to the active medium before we delve into the rate equations.

**Internal quantum efficiency,  $\eta_i$**  the fraction of terminal current that generates carriers in the active region. [4]

Since there are  $\eta_i I/q$  electrons per second being injected into the active region, we have that

$$G_{gen} = \frac{\eta_i I}{qV} \quad (5.2)$$



The recombination process is a bit more complicated and the total effect can be split up into four terms:

$$R_{rec} = R_{sp} + R_{nr} + R_l + R_{st} \quad (5.3)$$

where  $R_{sp}$  is the spontaneous recombination rate,  $R_{nr}$  is decay by nonradiative process,  $R_l$  is loss by charge carrier leak out of the active region and finally  $R_{st}$  is the net stimulated recombination (including both stimulated absorption and emission) which requires the presence of photons.

The first three terms refer to natural or unstimulated carrier decay processes. In the absence of photons or generation terms the carrier decay is a simple exponential decay with characteristic time  $\tau$ , so the first three terms can be combined as  $N/\tau$ , with  $\frac{1}{\tau} = \frac{1}{\tau_{sp}} + \frac{1}{\tau_{nr}}$  giving

$$R_{rec} = N \left( \frac{1}{\tau_{sp}} + \frac{1}{\tau_{nr}} \right) + R_{st}. \quad (5.4)$$

Combining all of our expressions we have

$$\frac{dN}{dt} = \frac{\eta_i I}{qV} - N \left( \frac{1}{\tau_{sp}} + \frac{1}{\tau_{nr}} \right) - R_{st}. \quad (5.5)$$

This is the first of the two important rate equations.

We now wish to construct a rate equation for the *photon density*  $N_p$ . Our reference point for this will be

$$\frac{dN_p}{dt} = \Gamma R_{st} + \Gamma \beta_{sp} R_{sp} - \frac{N_p}{\tau_p} \quad (5.6)$$

Where  $R_{st}$  and  $R_{sp}$  are the rates of recombination resulting in stimulated- and spontaneous emission respectively. These will be substituted by other expressions in due time. The last  $\frac{N_p}{\tau_p}$  term is the natural decay for photons including all mechanisms that could result in net loss of useful photons (absorption, scattering, etc.).  $\Gamma \equiv V/V_p$  is the *electron-photon overlap factor* also called the *confinement factor*, the active region volume occupied by electrons  $V$  divided by the, usually larger, volume occupied by photons,  $V_p$ . Thus the stimulated photon-generation rate is not simply  $R_{st}$  but  $\frac{V}{V_p} R_{st}$ .

In the case of the useful spontaneous photon generation rate, we multiply by an additional factor of  $\beta_{sp}$  which is defined as the ratio of useful vs. useless photons resulting from the random direction of emission, where only those hitting the optical mirrors at a small angle to the normal are useful ( $\beta_{sp}$  is of the magnitude  $10^{-4}$ ).

We also want to find a more suitable expression for  $R_{st}$  in terms of gain and photon volume density  $N_p$ . We define the gain for the active region

**Gain**,  $g$  the derivative of logarithm of photon density  $N_p$  as it passes through the medium [1]

That is,

$$g = \frac{d}{dz} \ln(N_p) = \frac{dN_p/dz}{N_p} \quad (5.7)$$

which can be solved as  $N_p(z) = N_{p0} \exp(gz)$  in which we can also recognize gain as the photon density growth rate per unit length. Stated slightly different:

$$N_p + \Delta N_p = N_p \exp(g\Delta z) \quad (5.8)$$

For sufficiently small  $\Delta z$ ,  $\exp(g\Delta z) \approx (1 + g\Delta z)$ . Using that  $\Delta z = v_g\Delta t$  where  $v_g$  is the group velocity, we find that  $\Delta N_p = N_p g v_g \Delta t$ . We can now deduce the generation term for the stimulated photon emission which is identical to the recombination rate of electrons resulting in net stimulated emission

$$\left(\frac{dN_p}{dt}\right)_{gen} = R_{st} = \frac{\Delta N_p}{\Delta t} = v_g g N_p \quad (5.9)$$

Rewriting the carrier equation (5.5) we get

$$\frac{dN}{dt} = \frac{\eta_i I}{qV} - N \left( \frac{1}{\tau_{sp}} + \frac{1}{\tau_{nr}} \right) - v_g g N_p \quad (5.10)$$

We note that the *first* term relates to the increase of charge carrier density as a direct result of the applied current, the *second* term relates to the loss of charge carriers due to both spontaneous emission and charge carrier leak to the surrounding material and the *third* term is the loss or gain due to the presence of photons. We see that negative gain will result in a positive third term visa versa. This is intuitive; once lasing kicks in, which is at positive gain, the stimulated emission of photons will result in a loss of charge carriers. On the other hand, just after the laser is turned on, the stimulated emissions has not yet reached a critical level, most photons present due to stimulated emission will likely be absorbed thereby creating charge carriers.

Finally invoking the substitution  $R_{sp} = \frac{N}{\tau_{sp}}$  and using the expression for  $R_{st}$  found above in (5.9) the photon rate equation (5.1) becomes:

$$\frac{dN_p}{dt} = \left[ \Gamma v_g g - \frac{1}{\tau_p} \right] N_p + \Gamma \beta_{sp} \frac{N}{\tau_{sp}} \quad (5.11)$$

We note that the *first* term relates to stimulated emission (high gain  $g$  during lasing) in the active region, the *second* term relates to loss as a result of natural “decay” (absorption) of photons in the active region and the *third* term relates to the increase of photons due to spontaneous emission of photons from electrons spontaneously moving from the conductive band to the valence band of the atoms in the active region.

We now have two coupled linear partial differential equations, (5.10) and (5.13), that can be solved numerically for the charge carrier density and photon density, for a given set of parameters and boundary conditions.

### 5.1.2 Simulating the rate equations for a simple laser

We will now numerically solve the rate equations, (5.10) and (5.13) with MATLAB using the following model for the gain:

$$g = \frac{g_0}{1 + \epsilon N_p} \ln \frac{N}{N_t r} \quad (5.12)$$

For equation (5.13) we define the contents of the square bracket as the stimulation factor:

**Stimulation factor**,  $\xi \equiv \Gamma v_g g - \frac{1}{\tau_p}$  The coefficient to  $N_p$  in  $N_p$ 's rate equation (5.13). The combined effect of the gain  $g$  and the natural photon decay  $\frac{N}{\tau_p}$ . Indicates the amount of stimulated emission at a specific time.

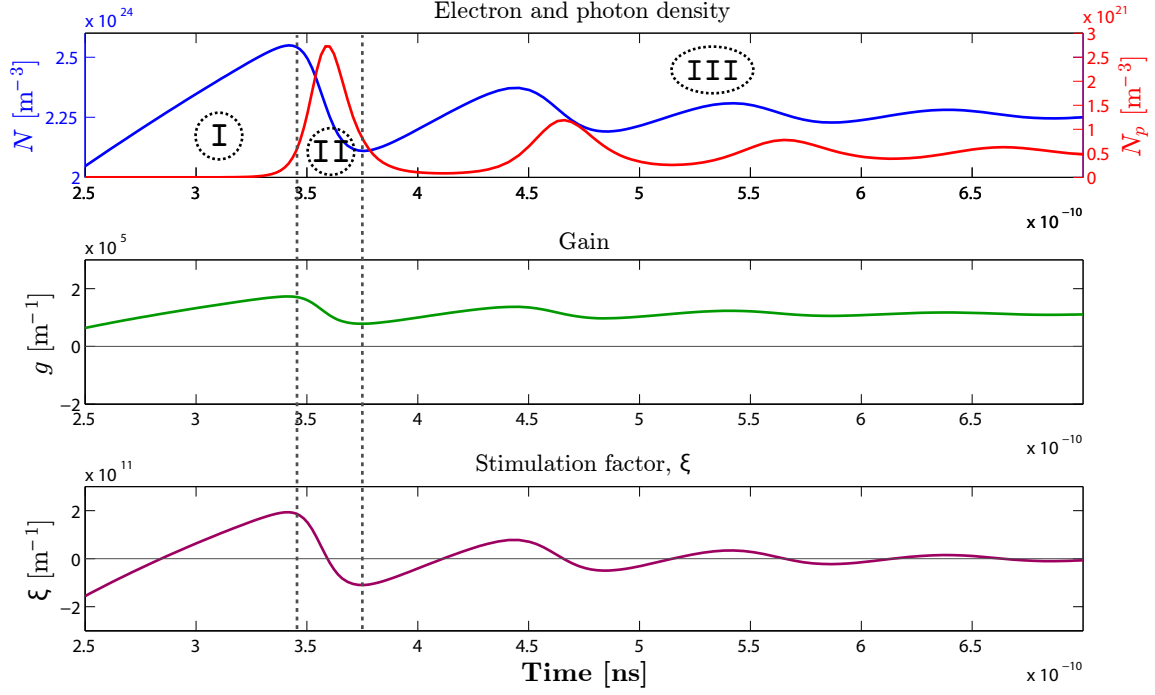


**Figure 5.1:**  $N(t)$ ,  $N_p(t)$ ,  $g(t)$  and  $\xi(t)$  on the same time-scale. REGION I: Spontaneous emission dominated until at the end REGION II: Stimulated emission dominated, active region achieves photon-oversaturation ( $g$  decreases,  $N_p$  reaches maximum) REGION III: Still stimulated emission dominated, going towards steady-state.

With this definition equation (5.13) can be written:

$$\frac{dN_p}{dt} = \xi N_p + \Gamma \beta_{sp} \frac{N}{\tau_{sp}} \quad (5.13)$$

We've chosen a set of realistic parameters to showcase the dynamics of the simple laser model, see 7.6. These parameters will be used for the rest of this subsection unless other is stated. We have obtained a numeric solution for  $N(t)$  and  $N_p(t)$ : Let us explore figure 5.1 in detail going from left to right on the time-axis. REGION I: Current is turned on,  $N$  rises because of the first term in (5.10).  $N_p$  remains low because the gain, depending logarithmically on  $N$ , remains low. Note that gain starts off negative, which cannot be seen in the chosen time interval, and changes sign at  $N = N_{tr}$ , see (5.12). Spontaneous photon emission continues to increase due to the growth of  $N$ , and eventually gets so large that the  $\xi$  term takes over and kick-starts the stimulated emission. This process is similar to a nuclear chain reaction;  $N_p$  undergoes faster-than-exponential growth. REGION I/II BOUNDARY: Because of gain's  $1/N_p$  dependency the gain and  $\xi$  maxes out while  $N_p$  continues its explosive growth. REGION II: The active media is oversaturated with photons and the current cannot replace electrons fast enough, thus  $g$  and  $\xi$  decreases as  $N_p$  reaches its maximum. The  $N_p$  maximum occurs more or less at the same time as  $\xi$  changes sign. This signifies that spontaneous emission is insignificant to the photon density  $N_p$  at this point. REGION III: In the  $N$ - and  $N_p$ -plot we notice the same pattern of  $N_p$  following the growth of  $N$  with a bit of delay resulting from the exactly the same mechanisms described for region I and II. We also note that the stimulation factor  $\xi$  oscillates between positive and negative, eventually settling on a value that results in  $\frac{dN_p}{dt} = 0$ .  $N$  and  $N_p$  also converges, resulting in the laser reaching a *steady state*.

Now if the current is lowered, all other parameters being equal, we might not achieve lasing. This

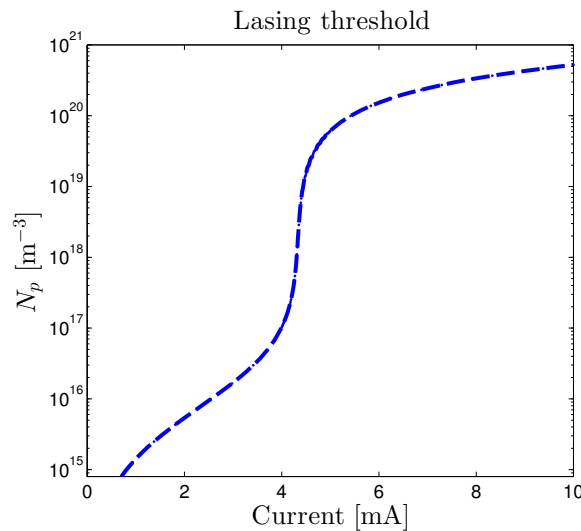


**Figure 5.2:** The lasing threshold; steady-state photon density is plotted for 150 different currents (chosen so there are more points around threshold). At approximately 4.3 mA lasing power increases three orders of magnitude from a very small fractional increase of input current. At currents lower than the threshold, the laser photon density is dominated spontaneous emission and at current higher than the threshold, by stimulated emission.

is due to the fact that the spontaneous emission rate must become higher than a certain threshold before the active medium gain reaches a value that results in a net gain of stimulated photons when a photon passes once through the active medium. This laser threshold current is characterized by a multiple orders-in-magnitude jump of photon density from much less than an order of magnitude of increase of input current.

Figure 5.2 shows the threshold current for lasing and how dramatic the steady-state photon density increases.

Another way to show this lasing vs. non-lasing and spontaneous vs. stimulated emission transition is to look at the actual time evolutions of photon densities of four different currents around the threshold current as in figure 5.3. Here we note the transients of the black and green curves, characteristic of lasing. However the green curve in 5.3 (a) shows us that lasing is not a truly discontinuous threshold phenomenon; there is current interval of sharp transition from non-lasing (blue and red) to lasing (black), but in between, a carefully increased current will give a very sudden but still continuous increase in laser power. We note in 5.3 (a) the blue photon density graph converges well below the blue dotted line. The blue dotted line is where it would have converged to under pure spontaneous emission, had photons not been lost to stimulated emission. In 5.3 (b) we see that the gain at this current  $I = 1.00$  mA never becomes positive, so the stimulated emission only takes away from the laser power (which is too low to be useful anyway). This happens because the stimulated emission has not reached a critical level to yield a net-gain of photons as they pass through the whole active region, but only takes away photons and creates charge carriers by absorption (last term in (5.10) is positive). As current is increased one of the indications that lasing is achieved is that photon densities converges to a steady-state level many orders of magnitude above the theoretical maximum from purely spontaneous emissions (the dotted lines), see the green and black curves. In the end we note that the gain appears to converge towards the same level, around  $10^5$ , once lasing is achieved no matter the current, however early higher gain for higher currents will result in an increased steady-state power.

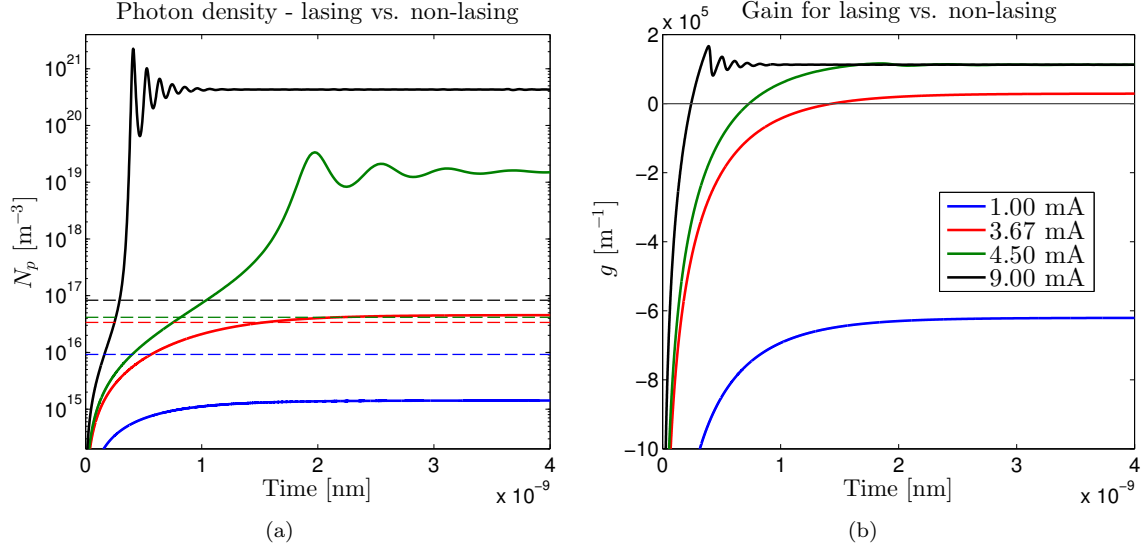


**Figure 5.3:** Photon density and gain for different currents just around the threshold current. The plot legend applies to both figures. (a) The laser reaching various steady-state photon densities for four different input currents around the threshold. The dotted colored lines indicates the respective steady-state densities, had the gain been zero, a maximum if there had only been spontaneous emission. These are obtained as the steady-state values for the rate equations with  $g_0 = 0$ . (b) The gain for the four different input currents

## 5.2 Implementation of quantum dot laser gain

At this point we have established a robust numerical model and we have carefully studied the rate equations, thus we have the theory necessary to advance to the study of the quantum dot laser. The main difference will be that a new gain model for quantum dot lasers have to be implemented.

For the new gain model we will look at a population of quantum dots, an ensemble, that are stacked in layers, much like in the figure back in the introduction, fig. 1.2. The material gain from this ensemble is given by a sum over all the individual QDs, where the important quantities of the sum are the electron-hole overlap integral (we elaborate this quantity soon), the dot volume and the ground state eigenenergy for the dots. Since a typical laser cavity can easily contain up to  $10^6$  QDs the sum is obviously problematic. However, the sum can be omitted by assuming that the QD volume size is described by a Gaussian distribution with a particular relative standard deviation and average volume that corresponds to an average ground state energy denoted  $\bar{E}_0$ . This assumption is justified if the ensemble consists of a sufficiently large number of independent quantum dots by virtue of the central limit theory [7] (any large population converges towards a Gaussian distribution). This assumption leads to the energetic broadening function [5]

$$P(\varepsilon, \sigma_E) = \frac{1}{\sigma_E \sqrt{2\pi}} \exp \left( -\frac{(\varepsilon - E_g - \bar{E}_0)^2}{2\sigma_E^2} \right), \quad (5.14)$$

where  $\sigma_E$  is the spectral width – the full width at half maximum. If we let  $\varepsilon = E_g + \bar{E}_0 = E_g + E_v + E_c$  (bandgap energy, valence band ground state energy and conduction band ground state energy), we obtain the simple relation  $P = \frac{1}{\sigma_E \sqrt{2\pi}}$  – this corresponds to letting the quantum dot laser operate at the energy that equals the difference between the valence band ground state and conduction band ground state plus the bandgap.

We will now further assume that electrons and holes injected into the QD active medium have the same capture time (the time it takes for an electron/hole to become confined in a QD). Also it is

assumed that carrier lifetime and carrier capture are independent of the ground state energy and that the dots do not couple. Lastly we will only concern us about the ground state of all QDs, which means that the total number of captured electrons distributed equally amongst all dots in the laser will be given by  $N = 2f_c N_D$ , where  $f_c$  denotes the Fermi-Dirac distribution, which describes the average number of fermions (electrons in this case) in a single-particle state (the ground state in this case) [3]. The quantity  $N_D$  is the total number of dots, and the factor 2 is due to the Pauli exclusion principle that allows only two electrons (of different spin) to be occupied in the same state. With all of the above-mentioned assumptions the material gain can be written [5]

$$g(\hbar\omega) = \frac{N - N_D}{N_D} C_g P(\hbar\omega, \sigma_E), \quad (5.15)$$

with the constant  $C_g$  given by

$$C_g = \frac{2\pi e^2}{m_e^2 \varepsilon_0 c n_r \omega} \frac{M^2}{V_0}, \quad (5.16)$$

where  $M$  is the electron-hole overlap integral,  $\varepsilon_0$  is the vacuum permittivity,  $c$  is the speed of light,  $n_r$  is refractive index of the active medium,  $\omega$  is the frequency of QD emitted light (corresponding to the energy gap between the electron ground state energy and the hole ground state energy plus the bandgap) and  $e$  is the elementary charge. It is seen from these expressions that the gain increases linearly with the carrier density from the minimum value  $-C_g P$  to the maximum value  $+C_g P$ , when all QDs ground states are filled with two electrons and two holes ( $N = 2N_D$ , the limiting value of  $N$ ). Note that  $N$  and  $N_D$  can either be regarded as absolute values or densities; this does not change the gain. For compatibility with the previously derived rate equations we will regard  $N_D$  as a density. In this new gain model the value of the carrier density  $N = N_D$  is equivalent to the quantity  $N_{tr}$  (called the transparency carrier density) in the old gain model.

### 5.2.1 Envelope wave function overlap integral of electron and hole

The overlap integral contained in (5.20) is loosely speaking a measure of the degree of how much the electron and hole wave functions overlap spatially. In defining the overlap integral we will distinguish between the electron wave function  $\psi_e$  and the hole wave function  $\psi_h$  with the quantum numbers  $n_e$  and  $n_h$ , respectively. The overlap integral can then be written

$$M = \int \bar{\psi}_e(\vec{x}, n_e) \psi_h(\vec{x}, n_h) \times \int \bar{\psi}_h(\vec{x}, n_h) \psi_e(\vec{x}, n_e). \quad (5.17)$$

It can be shown that this overlap integral will equal zero, whenever the angular quantum numbers are unequal, that is  $n_e \neq n_h$ . When  $n_e = n_h$  we can factor out the angular dependent term  $\exp(in\phi)$  (assuming azimuthal symmetry) in (5.17), which results in

$$M = 4\pi^2 \int_0^\infty \int_{-\infty}^\infty \bar{\chi}_e(z, r) \chi_h(z, r) r dr dz \times \int_0^\infty \int_{-\infty}^\infty \bar{\chi}_h(z, r) \chi_e(z, r) r dr dz. \quad (5.18)$$

Eq. (5.18) can now be used to calculate the overlap between the electron and hole wave function.

### 5.2.2 Optimization of gain from quantum dots

Based on the overlap integral from previous section we will now try to find the optimal dimensions of a QD for application in a QD laser. The QD gain is proportional to the constant  $C_g$  and therefore we will try to optimize this constant. Looking at the expression of  $C_g$ , (5.16), we see that the only variable parameters determining  $C_g$  are  $M$ ,  $V_0$  and  $\omega$  – the rest of the  $C_g$  expression consist only of physical quantities. Thus an optimization of  $\frac{M^2}{\omega V_0}$  will lead us directly to the quantum dot resulting in the highest possible gain.

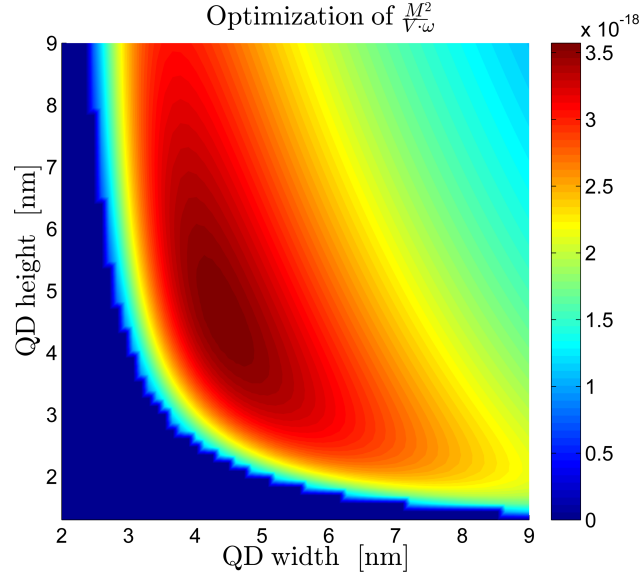


**Figure 5.4:** Data from optimization of QD laser gain. The slightly jagged profile on the light blue boundary is due to the looping resolution being limited; we have computed the optimization parameter for a total number of  $60 \times 60$  QDs (60 different heights and 60 different widths in the interval). Notice that the sharp shift from the optimum area to the dark blue area is a result of the electron wave function suddenly detaching and becoming unconfined for small heights and widths, making the overlap integral become very small for these QDs.

Such an optimization has been carried out by looping over a high number of different QDs ranging from 2 nm height/width to 15 nm height/width. The script for doing this extracts numerical solutions of  $\chi_e$  and  $\chi_h$ , normalizes the wave functions, calculates the overlap integral by numerical integration, and then finds the quantity  $M^2/\omega V_0$ . The  $\omega$  for a given QD is found by  $\varepsilon = \hbar\omega$ , where  $\varepsilon$  is, as earlier, set to  $E_g + E_v + E_c$  – the value of  $E_v$  and  $E_v$  are computed by the numerical model for the individual QD and the bandgap is set to  $E_g = 0.359$  eV. The data from running this script is plotted in fig. 5.4. The script can be found in app. 7.5.

From fig. 5.4 we see that there is an evident optimum. This optimum corresponds to a height of 4.56 nm and a width of 4.37 nm – the value of the overlap integral is found to be 0.624 for this particular QD.

### 5.2.3 Rate equations for quantum dot laser

We are now ready to simulate the quantum dot laser based on the new gain model 5.20. At this point however, we do not wish to make any assumptions about the quantum dot density  $N_D$ . We will therefore scale our gain- and rate equations by dividing with a factor  $N_D$ , effectively making

the QD-laser simulation independent of this  $N_D$ :

$$\tilde{N} = \frac{N}{N_D} \quad , \quad \tilde{I} = \frac{I}{N_D} \quad , \quad \tilde{N}_p = \frac{N_p}{N_D} \quad (5.19)$$

$$\Rightarrow \quad g = \frac{N - N_D}{N_D} C_g P \quad \longrightarrow \quad \boxed{g = (\tilde{N} - 1) C_g P} \quad (5.20)$$

$$\Rightarrow \quad \frac{dN}{dt} = \frac{\eta_i I}{qV} - N \left( \frac{1}{\tau_{sp}} + \frac{1}{\tau_{nr}} \right) - v_g g N_p \quad \longrightarrow \quad \boxed{\frac{d\tilde{N}}{dt} = \frac{\eta_i \tilde{I}}{qV} - \tilde{N} \left( \frac{1}{\tau_{sp}} + \frac{1}{\tau_{nr}} \right) - v_g g \tilde{N}_p} \quad (5.21)$$

$$\Rightarrow \quad \frac{dN_p}{dt} = \left[ \Gamma v_g g - \frac{1}{\tau_p} \right] N_p + \Gamma \beta_{sp} \frac{N}{\tau_{sp}} \quad \longrightarrow \quad \boxed{\frac{d\tilde{N}_p}{dt} = \left[ \Gamma v_g g - \frac{1}{\tau_p} \right] \tilde{N}_p + \Gamma \beta_{sp} \frac{\tilde{N}}{\tau_{sp}}} \quad (5.22)$$

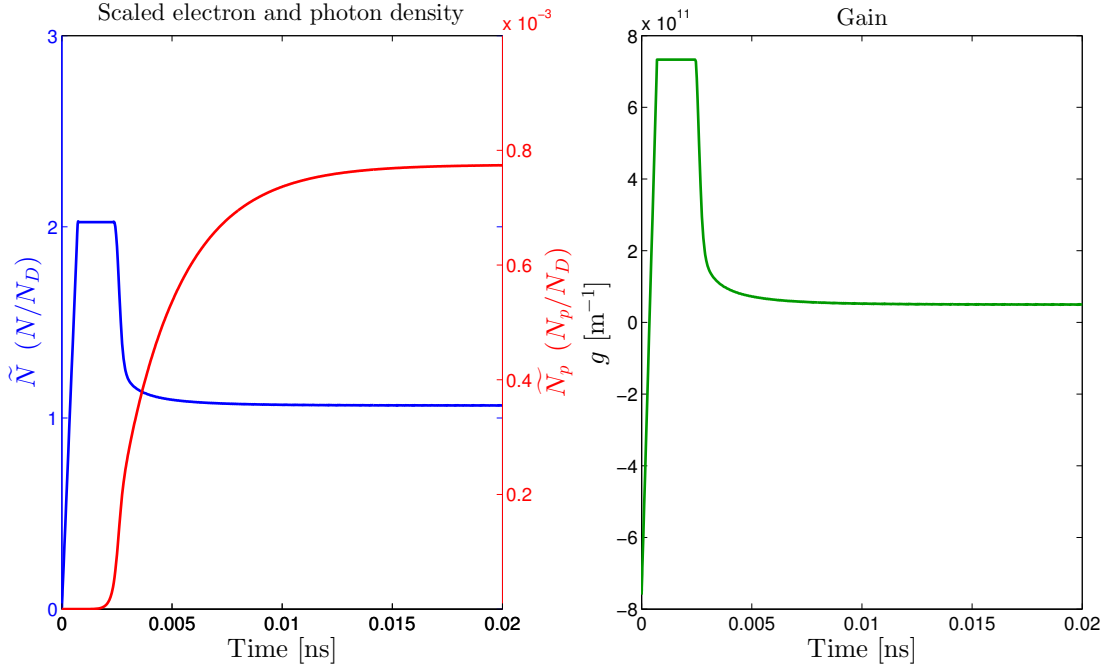


**Figure 5.5:** Scaled electron and photon densities  $\tilde{N}$  and  $\tilde{N}_p$  for the quantum dot laser simulation. Note how the timescale for steady-state is much smaller than in the first laser simulation. Also note how  $\tilde{N}$  saturates at 2 very early meaning that all the quantum dots are filled with electrons in the ground state. After the lasing gets going around 0.002 ns  $\tilde{N}$  drops as electrons are stimulated to emit photons. Steady-state is reached after about 0.2 ns. In our simple model the gain follows the scaled electron density, see (5.20).

To simplify we assume only the ground state is available for the electrons in the quantum dots. Because of the Pauli exclusion principle this means two possible quantum states; one spin up, one spin down. Therefore we must impose a limit on  $N$  so that  $N \leq 2N_D$  or  $\tilde{N} < 2$ . This is implemented together with the new gain model into the MATLAB simulation script. Note that the new rate equations, (5.21) and (5.22), both have the exact same form as the old ones – we just need to remind ourselves of the  $N_D$  scaling factor when we want to know the physically significant values.



Fortunately the laser simulation was successful with the new gain model with all other parameters being equal except the current. That is to say at parameters both realistic and optimized, lasing was achieved. See app. 7.7.:

The parameters using in the simulating of figure 5.5 makes it interesting because it uses the optimized value for  $C_g$  as presented in (5.16). If we drop the gain by an order of magnitude by adjusting  $C_g = 2.56 \times 10^8$  to  $C_g = 10^7$ , we get non-lasing as seen in fig. 5.6.

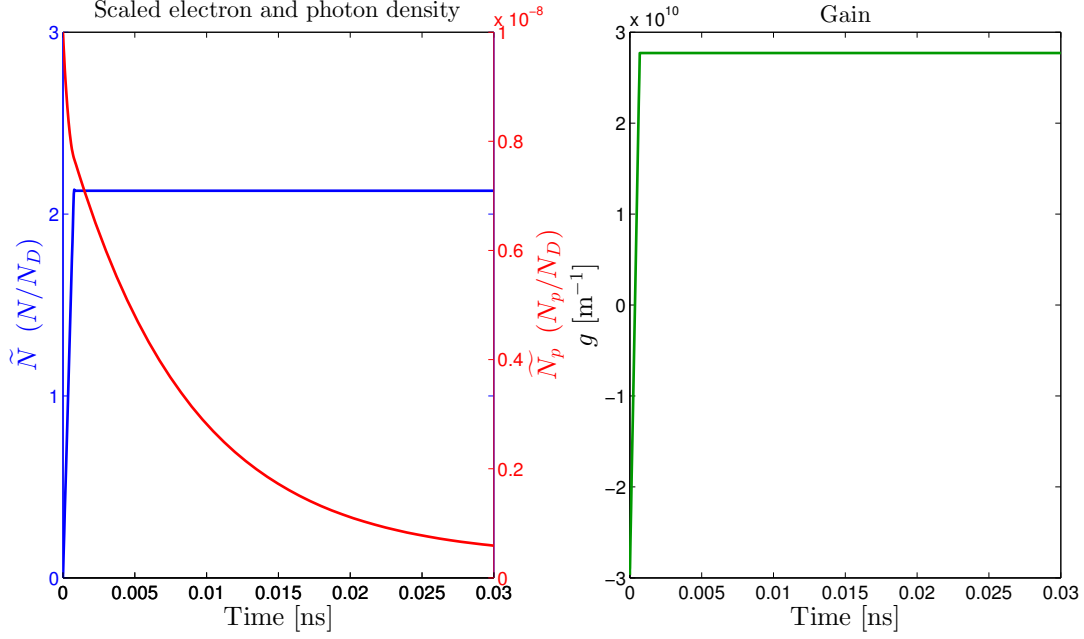


**Figure 5.6:** Scaled electron and photon densities  $\tilde{N}$  and  $\tilde{N}_p$  for the quantum dot laser simulation in a non-lasing situation.

Figure 5.6 shows us that no matter how much we saturate our quantum dots with electrons, the gain must still be high enough to achieve lasing. Finally we show how sensitive the system is by increasing  $C_g$  from  $C_g = 1 \times 10^7$  to  $C_g = 2 \times 10^7$  with a clear difference in photon density and definitely achieving lasing.

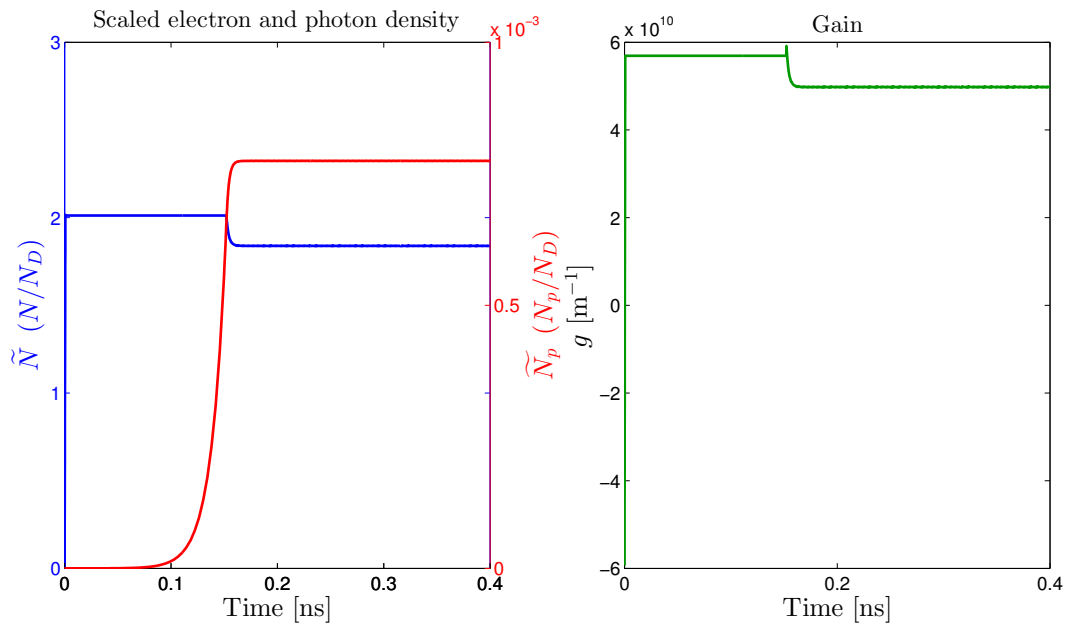


**Figure 5.7:** Scaled electron and photon densities  $\tilde{N}$  and  $\tilde{N}_p$  for the quantum dot laser simulation in a another lasing situation. This figure together with 5.6 is interesting because it shows how a very small difference in the  $C_g$  parameter and thereby gain, can mean the difference between lasing and non-lasing.

---

## Conclusion

We have demonstrated numerical computations of eigenenergies and wave functions of a conical quantum dot using COMSOL finite element simulations. We have found that the numerical model converge towards analytical solutions for the quantum well as the grid density in the mesh is improved, and we have also found that the error subject to using a limited computation domain is negligible. Based on the  $C_g$  factor in the expression for quantum dot laser gain, we have optimized the quantum dot dimensions to achieve maximum gain in a quantum dot laser. Finally we have shown that combining the gain expression from [5] and the laser rate equations using the optimized  $C_g$  value actually makes a working laser with realistic parameters.

## Appendix

### 7.1 Derivation for coefficient PDE form

Inserting  $c$ ,  $u$  and  $\vec{\beta}$  in (3.10)

$$\nabla \cdot \left( -\frac{\hbar^2}{2} \frac{1}{m_e} \frac{\partial \chi_n}{\partial r} \hat{\mathbf{r}} - \frac{\hbar^2}{2} \frac{1}{m_e} \frac{\partial \chi_n}{\partial z} \hat{\mathbf{z}} \right) - \frac{\hbar^2}{2} \frac{1}{m_e r} \frac{\partial \chi_n}{\partial r} \quad (7.1)$$

$$= -\frac{\hbar^2}{2} \left[ \frac{\partial}{\partial z} \left( \frac{1}{m_e} \frac{\partial \chi_n}{\partial z} \right) + \frac{\partial}{\partial r} \left( \frac{1}{m_e} \frac{\partial \chi_n}{\partial r} \right) + \frac{1}{m_e r} \frac{\partial \chi_n}{\partial r} \right] \quad (7.2)$$

The first term in the square brackets of (7.2) is also present in (3.9), so for the equality between (3.9) and (3.10) the remaining parts of both must be equal:

$$-\frac{\hbar^2}{2} \left[ \frac{\partial}{\partial r} \left( \frac{1}{m_e} \frac{\partial \chi_n}{\partial r} \right) + \frac{1}{m_e r} \frac{\partial \chi_n}{\partial r} \right] = -\frac{\hbar^2}{2} \frac{1}{r} \frac{\partial}{\partial r} \left( \frac{r}{m_e} \frac{\partial \chi_n}{\partial r} \right) \quad (7.3)$$

$$\Leftrightarrow \frac{\partial}{\partial r} \left( \frac{1}{m_e} \frac{\partial \chi_n}{\partial r} \right) + \frac{1}{m_e r} \frac{\partial \chi_n}{\partial r} = \frac{1}{r} \frac{\partial}{\partial r} \left( \frac{r}{m_e} \frac{\partial \chi_n}{\partial r} \right) \quad (7.4)$$

Expanding both sides by the rule of differentiation of a product, this can be written

$$\frac{\partial}{\partial r} \left( \frac{1}{m_e} \right) \frac{\partial \chi_n}{\partial r} + \frac{1}{m_e r} \frac{\partial \chi_n}{\partial r} + \frac{\partial^2 \chi_n}{\partial r^2} \frac{1}{m_e} = \frac{1}{r} \left( \frac{\partial}{\partial r} \frac{r}{m_e} \right) \frac{\partial \chi_n}{\partial r} + \frac{\partial^2 \chi_n}{\partial r^2} \frac{1}{m_e} \quad (7.5)$$

Removing the common term and differentiating the RHS again yields

$$\frac{\partial}{\partial r} \left( \frac{1}{m_e} \right) \frac{\partial \chi_n}{\partial r} + \frac{1}{m_e r} \frac{\partial \chi_n}{\partial r} = \frac{1}{r} \left( \frac{\partial}{\partial r} \frac{r}{m_e} \right) \frac{\partial \chi_n}{\partial r} \quad (7.6)$$

$$\Leftrightarrow \frac{\partial}{\partial r} \left( \frac{1}{m_e} \right) \frac{\partial \chi_n}{\partial r} + \frac{1}{m_e r} \frac{\partial \chi_n}{\partial r} = \left[ \frac{\partial}{\partial r} \left( \frac{1}{m_e} \right) + \frac{1}{m_e r} \right] \frac{\partial \chi_n}{\partial r}. \quad (7.7)$$

Since LHS and RHS are identical, the equation is true and we conclude that (3.9) and (3.10) are identical as well. The coefficient PDE (3.10) can now be directly implemented in COMSOL or other numerical tools in order to solve the Schrödinger equation (3.9).

### 7.2 Ineffectiveness of high mesh fineness

### 7.3 Envelope wave function

Script for obtaining the complete wave function for a Cartesian coordinate system.

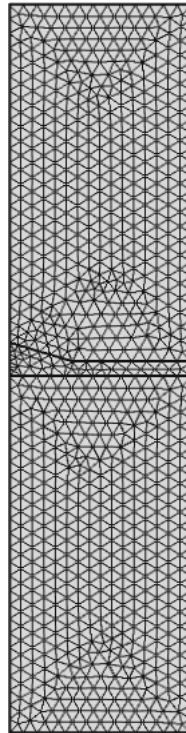


**Figure 7.1:** The fineness applied to the geometry is extra fine. As seen this way of increasing the number of grids does not adapt to the geometry.

```

1  for l=[0 4]
2      %% Params
3      h=10;
4      b=20;
5      % res=50;
6      QDRefin=3;
7      GaRefin=1;
8      meshLevel=5; %5 normal
9      dim=2;
10
11     %% model load
12
13     model=loadModel( dim,meshLevel,QDRefin,GaRefin );
14
15     model.param.set('V-Ga',0.697);
16     model.param.set('c-In','hbar^2/(2*0.027*m)');
17     model.param.set('c-Ga','hbar^2/(2*0.0665*m)');
18
19     %Specifying dimensions for QD
20     model.geom('geom1').feature('poll').set('y',[1;1;h]); %standard h -> 3.6
21     model.geom('geom1').feature('poll').set('x',[0;b;0]); %standard b -> 12
22
23
24     % Loading geometry and running mesh
25     model.geom.run;
26     model.mesh('mesh1').run;
27
28
29     model.param.set('l',1);
30
31     model.sol.run;
32

```

```

33
34 %Plotting
35 for mode=1
36     res=60;
37     [X,Y,Z]=meshgrid(linspace(-25,25,res),linspace(-25,25,res),linspace(-5,15,res));
38
39     % Danner matrix med r-koordinater
40     rCoords=reshape(sqrt(X.^2+Y.^2),1,[]);
41     %[ (x1,y1) , (x1,y2) , (x1,y3) , (x1,y4) , (x2,y1) ... ] — runs
42     %first all y in jumps of x, in jumps of z — that is for(z:, for(x:, for(y:,)))
43     RZcoords=[rCoords; Z(:)'];
44     U=mphinterp(model,'u','coord',RZcoords);
45
46
47     %Data export ini
48     % %      fid=fopen('C:\Users\Charles\AppData\Local\Programs\LLNL\VisIt ...
49     % %      2.5.2\data\QDL3.3D','w');
50     % %      fprintf(fid,['x',' y',' z',' value\n']);
51
52     %Indexing
53     XYZvalues=zeros(res,res,res);
54     count=1;
55     for k=1:res % Summer i z
56         for i=1:res % Summer i x
57             for j=1:res % Summer i y
58                 if X(i,j)>0 && Y(i,j)>0, koeff=atan(Y(i,j)/X(i,j)); end
59                 if X(i,j)<0 && Y(i,j)>0, koeff=pi+atan(Y(i,j)/X(i,j)); end
60                 if X(i,j)<0 && Y(i,j)<0, koeff=3*pi/2-atan(X(i,j)/Y(i,j)); end
61                 if X(i,j)>0 && Y(i,j)<0, koeff=2*pi+atan(Y(i,j)/X(i,j)); end
62                 if X(i,j)==0 && Y(i,j)==0, koeff=0; end
63                 if X(i,j)==0 && Y(i,j)>0, koeff=pi/2; end
64                 if X(i,j)==0 && Y(i,j)<0, koeff=3*pi/2; end
65                 if Y(i,j)==0 && X(i,j)>0, koeff=0; end
66                 if Y(i,j)==0 && X(i,j)<0, koeff=pi; end
67                 temp=cos(1*koeff)*U(mode,count);
68                 XYZvalues(i,j,k)=temp;
69                 %Skriver til export-fil
70                 %      fprintf(fid,'%f %f %f %f\n',X(i,j),Y(i,j),Z(1,1,k),temp);
71                 count=count+1;
72             end
73         end
74     end
75
76     %Lukker export fil
77     %      fclose(fid);
78
79     %      L=[];
80     %      for i=1:20*res+1,L=[L U(k,1+(i-1)*(20*res+1):i*(20*res+1))]; end
81     %      figure(1)
82     %      subplot(2,2,k)
83     %      surf(x,y,L)
84 end
85
86 %% Slices
87
88 [x,y]=meshgrid(0:1/res:20,-10:1/res:10);
89
90
91 % figure(1)
92 % count=0;
93 % for i=linspace(1,res,4)
94 %     count=count+1;
95 %     subplot(2,2,count)
96 %     surf(X(:, :, 1),Y(:, :, 1),XYZvalues(:, :, int8(i)), 'LineStyle', 'none');
97 % end
98

```



## 7.4 Plots for probability density function

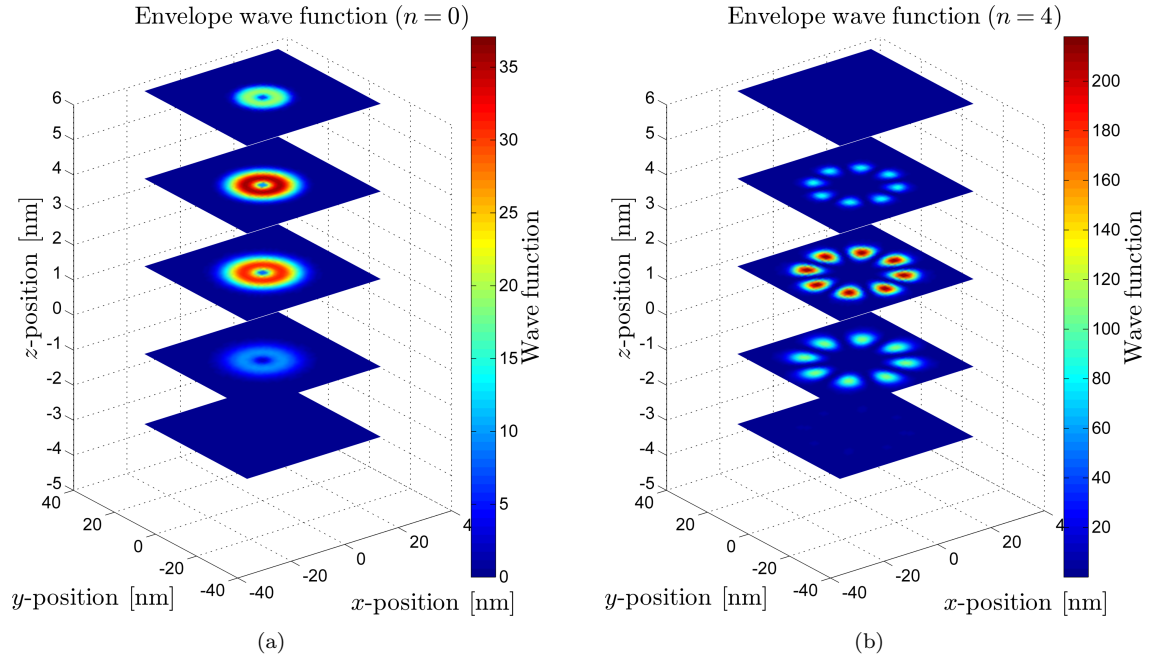


**Figure 7.2:** Horizontal slices of the probability density function multiplied by  $r$  (also referred to as the probability integrand  $|\psi(\vec{x})|^2 \cdot r$ ) for  $n = 0$  and  $n = 4$ . Due to the angular dependency  $\exp(in\phi)$  the quantum number  $n$  will give rise to exactly  $n$  oscillations in a full azimuthal rotation of  $2\pi$ . (a) Ground state belonging to  $n = 0$ , the eigenenergy is found to be  $E = 0.1223$  eV. Notice that the peak is no longer at  $r = 0$ . (b) Ground state for  $n = 4$ , eigenenergy is  $E = 0.3517$  eV. Notice that precisely 4 oscillations are completed in a full azimuthal rotation.

## 7.5 Script for optimization of quantum dot laser gain

```

1 % function [M,R,Rh,x,y,lambda,lambdah]=QDoverlapFunc(model,mode,h,b,res,dim)
2 % function [M,R,Rh,x,y,lambda,lambdah]=QDoverlapFunc_medRogRh(model,mode,h,b,res,dim)
3 %% Initialization
4
5 tic
6 clear all
7 close all
8
9 %Smart save
10 load('globalcount');
11 globalcount=globalcount+1;
12 save('globalcount','globalcount');
13 savdir=sprintf('datafiler/%s','h_b_loop3_extended');
14 mkdir(sprintf('%s/%i',savdir,globalcount))
15
16 fprintf('savefolder is numbered %i\n',globalcount);
17
18 %Data export ini
19 fid=fopen(sprintf('%s/%i/%s',savdir,globalcount,'data.dat'),'w');
20 %Dataset with forced M=0
21 fidMod=fopen(sprintf('%s/%i/%s',savdir,globalcount,'dataMod.dat'),'w');
22
23

```



```

24
25 % Loop params
26 % N=3;
27
28 % [h,b]=meshgrid(linspace(2,7,3*N),linspace(2,8,N));
29 hint=linspace(2,9,40);
30 bint=linspace(7,14,40);
31 % bint=[2 5 15];
32 % hint=[2 5 15];
33 % bint=7.18;
34 % hint=2;
35
36 % Parameters
37 meshLevel=4; % 5 er normal
38 QDRefin=3;
39 GaRefin=1;
40 mode=1;
41 res=250;
42 dim=2;
43
44 save(sprintf('%s/%i/%s',savdir,globalcount,'parameters'));
45
46 count1=0;
47 % count2=0;
48
49 % Loop
50 fig=figure('visible','off');
51 for b=bint %gennemlber b, bredden
52     model=loadModel( dim,meshLevel,QDRefin,GaRefin );
53     % count2=0;
54     mkdir(sprintf('%s/%i/b-%0.2f',savdir,globalcount,b));
55     % h & b Loop
56     for h=hint %gennemlber h, hiden
57
58         [M,R,Rh,x,y,lambda,lambdah]=QDoverlapFunc_medRogRh(model,mode,h,b,res,dim);
59
60         fprintf(fid,'%f\t',M);
61         % Forced m=0
62         [maxval, maxpos]=max(R(:));
63         [maxrow, maxcol]=ind2sub(size(R),maxpos);
64         Minterp=TriScatteredInterp(x(:),y(:),R(:));
65
66         if x(maxrow,maxcol)>b || Minterp(x(end),0)>1/10*maxval
67             fprintf(fidMod,'%f\t',0);
68         else
69             fprintf(fidMod,'%f\t',M);
70         end
71
72         subplot 221
73         surf(x,y,R)
74         shading interp
75         title(sprintf('E. h: %0.3f, b: %0.3f, M: %0.5f',h,b,M));
76
77         subplot 223
78         surf(x,y,R)
79         title(sprintf('Lambda: %0.5f',lambda))
80         shading interp
81         view(2)
82
83         subplot 222
84         surf(x,y,Rh)
85         title('Eh')
86         shading interp
87
88         subplot 224
89         surf(x,y,Rh)
90         title(sprintf('Lambda: %0.5f',lambdah))

```

```

91     shading interp
92     view(2)
93
94     export_fig('fig',sprintf('%s/%i/b_%0.2f/h_%0.2f_b_%0.2f',savdir,globalcount,b,h,b),'-png','-m
95
96     %         count2=count2+1;
97     %         if mod(count2,2)==0, fprintf('%i\n',count2); end
98
99     end
100    %         fprintf(fid,'%f\t', arrayfun( ...
101    %             @(x)QDoverlapFunc_medRogRh(model,mode,x,b(i),res,dim),h(1,:)) );
102    fprintf(fid,'\n');
103    fprintf(fidMod,'\n');
104
105    count1=count1+1;
106    fprintf('OUTER LOOP, compl. iter. # %i\n',count1);
107
108
109 end
110
111
112 fclose(fid);
113 fclose(fidMod);
114
115 %% Surf plot
116
117 matM=transpose(importdata(sprintf('%s/%i/%s',savdir,globalcount,'data.dat')));
118 figure(2)
119 [bmesh,hmesh]=meshgrid(bint,hint);
120 surf(bmesh,hmesh,matM);
121 hgsave(sprintf('%s/%i/%s',savdir,globalcount,'M_surf'))
122 rotate3d on
123
124 winopen(sprintf('%s/%i',savdir,globalcount))
125
126 toc
127
128 function [M,R,Rh,x,y,lambda,lambdah]=QDoverlapFunc_medRogRh(model,mode,h,b,res,dim)
129 % Note that 'mode' refers to the angular momentum quantum number
130 %% Initialisering
131
132 %% Opstning af polygon, standardpolygon [0,0,3.6]
133 model.geom('geom1').feature('pol1').set('y',[1;1;h]); %standard h -> 3.6
134 model.geom('geom1').feature('pol1').set('x',[0;b;0]); %standard b -> 12
135
136
137
138 % Indlser geometry og krer mesh
139 model.geom.run;
140 model.mesh('mesh1').run;
141
142 %Antal mesh
143 % meshdata = mphmeshstats(model,'mesh1');
144 % meshelem=meshdata.numelem(2);
145
146
147
148 %% Solver function call
149 %
150 % [R,x]=QDsolveFun2D(model,mode,submode,VGa,cIn,cGa,res,dim)
151 %
152
153 %Electron -----
154 [R,x,y,lambda]=QDsolveFun2D(model,mode,1,0.697,'hbar^2/(2*0.027*m)','hbar^2/(2*0.0665*m)',res,dim);
155
156
157 %Hole -----

```

```

158 [Rh,~,~,lambdah]=QDsolveFun2D(model,mode,1,0.368,'hbar^2/(2*0.34*m)','hbar^2/(2*0.38*m)',res,dim);
159
160
161 %% Output overlap value
162
163 %Computes int(r*Fe(*)*Fh)
164 int1 = 0;
165 for k=1:res
166     for j=1:res
167         int1=int1+conj(R(j,k))*Rh(j,k)*x(j,k);
168     end
169 end
170 int1=int1*(25*dim*75*dim/(res*res));
171
172 %Computes int(r*Fe*Fh(*))
173 int2 = 0;
174 for k=1:res
175     for j=1:res
176         int2=int2+R(j,k)*conj(Rh(j,k))*x(j,k);
177     end
178 end
179 int2=int2*(25*dim*75*dim/(res*res));
180
181 %Final calculation
182 M=4*pi^2*int1*int2;
183
184 end
185
186
187
188 function [R,x,y,lambdah]=QDsolveFun2D(model,mode,submode,VGa,cIn,cGa,res,dim)
189
190 % Parameters -----
191
192 model.param.set('V-Ga',VGa);
193 model.param.set('c-In',cIn);
194 model.param.set('c-Ga',cGa);
195
196
197
198 % Beregner lsning -----
199
200 model.param.set('l',mode);
201 %     model.geom.run;
202 %     model.result('pgl').run;
203 %     model.result.dataset('dset1').run;
204 model.sol.run;
205 %     model.sol('sol1').runAll;
206 % mphglobal(model,'lambda')
207
208 lambda=mphglobal(model,'lambda');
209 lambda=lambda(1);
210
211 %Opbygger 2d matrix -----
212
213 [x,y]=meshgrid(linspace(0,dim*25,res),linspace(-25*dim,50*dim,res));
214 U=mphinterp(model,'u','coord',[x(:)';y(:)']);
215 R=reshape(U(submode,:),res,res);
216
217 %Normalisering
218 total = 0;
219 for k=1:res
220     for j=1:res
221         total=total+R(j,k)^2*x(j,k);
222     end
223 end
224 total=total*(25*dim*75*dim/(res*res))*2*pi;

```

```

225 koeff=sqrt(1/total);
226
227 R=R*koeff;
228
229
230 end

```

## 7.6 Parameters for rate equations simulation

```

1  vg=1e8;
2  etai=0.8;
3  V=(300*0.016)*10^(-18);
4  Gamma=0.032;
5  taup=2.77e-12;
6  tausp=0.5e-9;
7  taunr=1e-3;
8  tau=(1/tausp+1/taunr)^(-1);
9  betasp=1e-4;
10 i=1e-2; % Standard I: i=10e-3
11 q=1.602e-19;
12 g0=5e5; % Standard g0=1.8e5;
13 epsilon=1.5e-23;
14 Ntr=1.8e24;
15 ts=0.25e-9
16 tf=0.7e-9;

```

## 7.7 Parameters and script for QD rate equations simulation

```

1
2 %% Real values
3 figure(1);
4 clf
5
6 global vg etai V Gamma taup tausp taunr tau betasp i q Cg P gMat tMat
7
8 % FRIE PARAMETRE
9 i=7*(300*0.016)*10^(-18)*1.602e-19*5e11;
10 tf=2e-11;
11
12 %%Initialisering
13
14 Cg=2.56e8/3.37; %(refractive index included)
15
16 % TJEK
17 taunr=1e-3; %1e-12;
18 tausp=0.5e-9;
19 tau=(1/tausp+1/taunr)^(-1); %+1/taunr
20 taup=2.77e-12;
21 etai=0.8;
22 V=(300*0.016)*10^(-18);
23 q=1.602e-19;
24 P=7.25;
25 Gamma=1e-4;
26 betasp=1e-4;
27 vg=1e8;
28
29
30 % Solver
31
32 % options = odeset('RelTol',1e-9);%,'AbsTol',[1e2, 1e2]

```

```

33 options = odeset('AbsTol',[1e-30, 1e-30]);
34 [t,y]=ode45(@rateEqGain,[0 tf],[1e-8 1e-8],options);
35 % [t,y]=ode45(@rateEq,[0 20],[1 0.1]);
36
37 % Plot af N og Np
38 clf
39 subplot 121
40
41 [AX,H1,H2] = plotyy(1e9*t,y(:,1),1e9*t,y(:,2));
42 title('Scaled electron and photon density','Interpreter','Latex','fontsize',18)
43 set(AX(1),'fontsize',14)
44 set(AX(2),'fontsize',14)
45 grid off
46 set(AX,'xlim',[0,1e9*tf]);
47 set(AX(1),'ylim',[0 3]);
48 set(AX(1),'YTick',[0 1 2 3]);
49 %set(AX(2),'ylim',[0 1e-3]);
50 set(AX(2),'YTick',1e-3*[0.2 0.4 0.6 0.8]);
51 set(AX(1),'ycolor','b')
52 set(AX(2),'ycolor','r')
53 ylabel(AX(1),'$\widetilde{N} \backslash, \backslash, \dots$'
54         '\left(N/N_D\right)$','fontsize',20,'fontweight','bold','Interpreter','Latex')
55 ylabel(AX(2),'$\widetilde{N}_p \backslash, \backslash, \dots$'
56         '\left(N_p/N_D\right)$','fontsize',20,'fontweight','bold','Interpreter','Latex')
57 xlabel('Time [ns]','fontsize',20,'Interpreter','Latex')
58
59 set(H1,'color','blue','LineWidth',2)
60 set(H2,'color','red','LineWidth',2)
61
62 %Plot af gain
63
64 gain=zeros(length(t),1);
65 for j=1:length(t)
66     if y(j,1)<2
67         gain(j)=(y(j,1)-1)*Cg;
68     else
69         gain(j)=gain(j-1);
70     end
71 end
72
73 subplot 122
74 plot(1e9*t,gain*vg*Gamma,'color',[0 0.6 0],'LineWidth',2);
75 title('Gain','Interpreter','Latex','fontsize',18)
76 set(gca,'XTick',[0 0.005 0.01 0.015 0.02])
77 set(gca,'FontSize',14)
78 ylabel('$g \backslash, \backslash, \dots$'
79         '[$\mathrm{m}^{-1}$]','$','fontsize',20,'fontweight','bold','Interpreter','Latex')
80 xlabel('Time [ns]','fontsize',20,'Interpreter','Latex')
81
82 sprintf('N: %0.5f , Np: %0.5f , g: %0.5f',max(y(:,1)),max(y(:,2)),max(gain(:)))
83
84 function eqns=rateEqGain(tt,y) %vg,etai,V,Gamma,tau,taup,Rsp,i,q,g,betasp,tausp
85
86 global vg etai V Gamma taup tausps tau betasp i q g Cg Nd gMat tMat P
87
88 % Gain
89
90 g =(y(1)-1)*Cg*P;
91
92
93
94 % N og Np
95 eqns=zeros(2,1);
96 eqns(1)=etai*i/(q*V)-y(1)/tau-vg*g*y(2); % afledte af n

```

```
97 eqns(2)=(Gamma*vg*g-1/taup)*y(2)+Gamma*betasp*y(1)/tausp; % afledte af np
98
99 if y(1) ≥ 2 && eqns(1)>0
100     eqns(1)=0;
101 end
102
103 end
```

## References

- [1] Gain (lasers) - definition. [http://en.wikipedia.org/wiki/Gain\\_\(laser\)#Definition](http://en.wikipedia.org/wiki/Gain_(laser)#Definition). [accessed 8-January-2013].
- [2] amit.science. How does a laser work. <http://www.winnerscience.com/science/physics/laser-physics/how-does-a-laser-work/>, 2012. [accessed 7-January-2013].
- [3] B.H. Bransden and C.J. Joachain. *Introduction to quantum mechanics*. Longman Scientific & Technical, 1989.
- [4] Larry A. Coldren, Scott W. Corzine, and Milan L. Mašanović. *A Phenomenological Approach to Diode Lasers*, chapter 2, pages 45–90. John Wiley & Sons, Inc., 2012.
- [5] Marius Grundmann and Dieter Bimberg. Gain and threshold of quantum dot lasers: Theory and comparison to experiments. *Japanese Journal of Applied Physics*, 36(Part 1, No. 6B):4181–4187, 1997.
- [6] K. Jacobi. Atomic structure of inas quantum dots on gaas. *Progress in Surface Science*, 71:196, 2003.
- [7] R.A. Johnson, I. Miller, and J.E. Freund. *Miller & Freund's Probability and Statistics for Engineers*. Prentice Hall, 2011.
- [8] R V N Melnik and M Willatzen. Bandstructures of conical quantum dots with wetting layers. *Nanotechnology*, 15(1):1, 2004.
- [9] Dr. M.Premasundaran and Dr. A.L. Dawar. Types of lasers. <http://www.worldoflasers.com/lasertypes.htm>. [accessed 7-January-2013].
- [10] Tim Harper Paul Holister, Cristina Román Vas. Quantum dots. [http://www.romnet.net/ro/e-newsletter/e-newsletter13/FreeNanotechnology-download/quantum\\_dots\\_WP.pdf](http://www.romnet.net/ro/e-newsletter/e-newsletter13/FreeNanotechnology-download/quantum_dots_WP.pdf). [accessed 16-January-2013].
- [11] Wikipedia. Quantum dots # fabrication. [http://en.wikipedia.org/wiki/Quantum\\_dot#Fabrication](http://en.wikipedia.org/wiki/Quantum_dot#Fabrication). [accessed 16-January-2013].
- [12] Wikipedia. Stranski–krastanov growth. [http://en.wikipedia.org/wiki/Stranski%E2%80%93Krastanov\\_growth](http://en.wikipedia.org/wiki/Stranski%E2%80%93Krastanov_growth). [accessed 16-January-2013].
- [13] S.S. Zumdahl. *Chemical Principles*. Brooks/Cole, 2009.